Journal Pre-proof

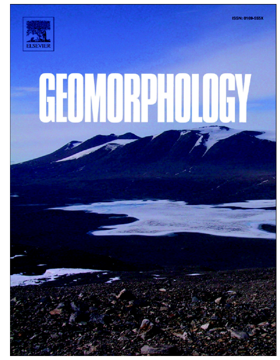

Machine-learning classification of debris-covered glaciers using a combination of Sentinel-1/-2 (SAR/optical), Landsat 8 (thermal) and digital elevation data

Haireti Alifu, Jean-Francois Vuillaume, Brian Alan Johnson, Yukiko Hirabayashi

PII: S0169-555X(20)30338-X

DOI: https://doi.org/10.1016/j.geomorph.2020.107365

Reference: GEOMOR 107365

To appear in: *Geomorphology*

Received date: 22 May 2020

Revised date: 26 July 2020

Accepted date: 26 July 2020

Please cite this article as: H. Alifu, J.-F. Vuillaume, B.A. Johnson, et al., Machine-learning classification of debris-covered glaciers using a combination of Sentinel-1/-2 (SAR/optical), Landsat 8 (thermal) and digital elevation data, *Geomorphology* (2020), https://doi.org/10.1016/j.geomorph.2020.107365

Machine-learning classification of debris-covered glaciers using a combination of Sentinel-1/-2 (SAR/optical), Landsat 8 (thermal) and Digital elevation data

Haireti Alifu[1]*, Jean-Francois Vuillaume[2], Brian Alan Johnson[3], and Yukiko Hirabayashi[4]

1 Department of Civil Engineering, Shibaura Institute of Technology, 3–7-5, Toyosu, Kotoo-ku, Tokyo, 135-8548, Japan; Tel: +81-03-5859-8353; E-Mail: haireti.alifu.f4@sic.shibaura-it.ac.jp
2 Center for Earth Information Sciences and Technology, CEIST, Japanese Agency for Marine-Earth Science and Technology, JAMSTEC; 3173-25 Showa-machi, Kanazawa-ku, Yokohama Kanagawa 236-0001, Japan: E-Mail: vuillaume@jamstec.go.jp
3 Institute for Global Environmental Strategies (IGES), 2108-11 Kamiyamaguchi, Hayama, Kanagawa, 240-0115, Japan; Tel: +81-046-855-3875; E-Mail: johnson@iges.or.jp
4 Department of Civil Engineering, Shibaura Institute of Technology, 3–7-5, Toyosu, Kotoo-ku, Tokyo, 135-8548, Japan; Tel: +81-03-5859-8353; E-Mail: hyukiko@shibaura-it.ac.jp
*Correspondence: haireti.alifu.f4@sic.shibaura-it.ac.jp and hairetialifu@outlook.com;

Abstract

Debris cover on glacier surfaces hampers the accurate detection of debris-covered ice using traditional techniques based on image band ratios. Therefore, this study tests a new automatic classification scheme for hierarchical mapping of glacier surfaces based on machine learning classifiers including k-nearest neighbors (KNN), support vector machine (SVM), gradient boosting (GB), decision tree (DT), random forest (RF) and multi-layer perceptron (MLP). Several raster layer combinations (synthetic aperture radar (SAR) coherence image derived from Sentinel-1 data, visible near-infrared to short wave infrared bands from Sentinel-2, thermal information from Landsat 8 and geomorphometric parameters from the Advanced Land Observing Satellite (ALOS) World 3D 30 m mesh (AW3D30) digital elevation model) were tested to delineate the debris-covered glaciers in the Gilgit-Baltistan, Pakistan and Shaksgam valley, China. The highest over classification accuracy (97%) was obtained using the RF classifier (followed by the GB and SVM with radial basis function kernel) and utilizing all of the multisensor Sentinel/Landsat/ALOS data. Notably, the RF classifier showed to be robust to parameter settings, fast and accurate for mapping debris-covered ice. GB classifier showed similar performance as RF despite it has a moderately lower accuracy compared to RF. Although SVM classifier has a slower in the speed of tuning hyper-parameter, it still performs the third-best classification accuracy. As the multisensory data we used is freely and (near-)globally available, our methodology potentially could be applied for precise delineation of debris-covered glaciers in other areas.

Keyw*ords: Debris-covered glacier, machine learning classifiers, Sentinel1&2, Landsat8, AW3D30, geomorphometric parameters*

1. Introduction

Runoff from glaciers is an important freshwater resource for humans, wildlife, and vegetation in dry climate domain regions, and also allows for hydropower generation (Pritchard, 2019). In the context of rising global temperatures, monitoring of glaciers over time is particularly important to help understand the effects of global warming (Haeberli et al., 2007). Repeated measurements over a long time period are needed for long-term analysis of changes in glacier extent (Bolch et al., 2012; Alifu et al., 2018), glacier velocity (Altena et al., 2019), glacier debris thickness (Schauwecker et al., 2015), and glacier mass balance (Marzeion et al., 2015; Brun et al., 2017) at local to global scales. Moreover, monitoring of intra-annual (seasonal) glacier dynamics is also necessary for hydrological modeling and the estimation of seasonal water availability (Pritchard, 2019).

Accurate measurements of glacier areas are only feasible to obtain by remote sensing, as upper glacier boundaries are often inaccessible. The first Satellite-based glacier inventory - the Randolph Glacier Inventory (RGI) - contains a collecting of glacier outlines globally (excluding the Greenland and Antarctic ice sheets) created from satellite images around 1999 using both manually and semi-automatically derived outlines (such as from band ratio or normalized indices) (Pfeffer et al., 2014). Although (semi-)automated mapping of debris-free glacier can be done at quite high levels of accuracy based on the unique spectral features of glaciers compared to the other rocky mountain landscape, it was quickly realized that identification of glaciers covered by rocks and other debris was a major challenge (Bishop et al., 2001; Paul et al., 2004; Ranzi et al., 2004; Bolch et al., 2007; Racoviteanu et al., 2009; Shukla et al., 2010a; Bhambri et al., 2011).

Debris-covered glaciers are common features in most of the high mountainous areas of the world (Kirkbride, 2011), and are widely found in the mountains of Himalaya (Bhambri et al., 2011), Karakoram (Copland et al., 2011), Alaska (Le Bris et al., 2011), New Zealand (Röhl, 2008), Caucasus (Stokes et al., 2007), and parts of the Andes (Racoviteanu et al., 2008). The spatial distribution of debris cover, and the varying thickness of the debris cover on the glacier surface, can change glacier ablation and thereby glacier responses to climate change differently. Therefore, it is essential to monitor these debris-covered glaciers over time to better understand how they are changing. Past studies based on field observations indicated that a thin debris layer enhances the underneath ice melting, whereas a heavy debris layer slows down the ablation (Östrem, 1959; Nakawo and Young, 1982; Nicholson and Benn, 2006). Thus, monitoring of the debris-cover glacier area and its change are essential to generate accurate model/accurate estimates of discharge, fresh-water availability, and sea-level rise. Also, it is important to realize how the debris-covered glacier's ablation can be associated with the glacial lake formation, as glacial lake outburst floods can pose extreme risks to downstream populations (Benn et al., 2012).

Automated classification of debris-covered glaciers still remains a challenging task because it is hard to detect the glacier boundary under the debris cover (debris cover has similar spectral characteristic to the adjacent rocky mountainous surface). Various methods for mapping of debris-covered glaciers have been developed and tested, but most are based on semi-automatic classification methodologies, and require manual editing of the initial classification results to produce an accurate map (Paul et al., 2004; Shukla et al., 2010a; Bhambri et al., 2011; Racoviteanu and Williams, 2012; Rastner et al., 2013; Alifu et al., 2015;

Alifu et al., 2018). Nonetheless, several studies have performed fully automatic delineation of debris-covered glacier using Synthetic Aperture Radar (SAR) data (Huang et al., 2014; Lippl et al., 2018) or a combination of SAR, optical and topographic data (Robson et al., 2015; Zhang et al., 2019). The studies by Brenning (2009), Huang et al. (2014) and Lippl et al. (2018) all involved the mapping on a single glacier, and achieved classification accuracies of around 95%. Robson et al. (2015) obtained a classification accuracy of nearly 85% for debris-covered ice over a relatively larger (~800 km^2) glacierized area. Recently, Zhang et al. (2019) used a random forest classifier to classify debris-covered glaciers based on topographic and textural features using Landsat 8 imagery and digital elevation model (DEM) data. However, these automatic classification methods were mostly optimized for mapping glaciers in a small study area, or achieved lower classification accuracies in the case of large glacierized areas and classifier algorithms without optimization of hyper-parameters (Huang et al., 2014; Robson et al., 2015; Lippl et al., 2018). Nevertheless, it is important to note from previous studies that geomorphometric parameters such as slope, plan curvature and profile curvature (Paul et al., 2004; Bolch and Kamp, 2005), SAR features such as coherence pattern (Huang et al., 2014), and optical/thermal features (Shukla et al., 2010b) were all found to provide useful information for accurate mapping of debris-covered glaciers. However, they are not fully utilized in previous studies on debris glacier classification.

The main objectives of this research are to: (i) present an automated machine learning classification scheme for the hierarchical mapping of debris-covered glaciers over a large area based on the integration of SAR coherence data, optical data, thermal data and topographic data, and (ii) assess the effectiveness of several machine learning classifiers (including k-nearest neighbors, support vector machine, gradient boosting, decision tree, random forest, and multi-layer perceptron) for glacier mapping using the multi-sensor remote sensing data.

2. Study area and datasets

2.1 Study area

The proposed method was examined in the North-western Karakoram region of Gilgit-Baltistan, Pakistan (Test1, Fig. 1a) and Shaksgam Valley (Test2, Fig. 1b) which is located on the northern side of the Karakoram mountain range in western China. Nearly 2000 km^2 of the area in Test1 is covered by glaciers. Debris-covered glaciers, with varying degrees of debris thickness, are common in the Test1 region (Gardner and Hewitt, 1990; Senese et al., 2018). The elevations of the debris-covered glaciers in Test1 area range from 2300 m to7700 m, and most of glaciers have a width of 0.2 − 2.4 km and extend from 0.5 − 60 km in length. Moreover, the objective glacier extents vary from 0.5 to 300 km^2. Debris cover can be found in any orientation of glacier surface, size (small to large) and slope (12-40 degrees). On the other hand, Test2 has a glacierized area of 1200 km^2. Elevation ranges of the glacier in Test2 are from 3200 m to 8611 m (second highest peak in the world, K2). Varying degrees of debris cover on the glacier surface is also common features in the Test2 area, and most of them are covered by thick rocky debris layer (Shi et al., 2008). Monitoring glaciers is particularly important in the study areas due to the millions of people downstream who are reliant on glacier meltwater for sanitation, irrigation, and hydropower generation. Previous studies reported that the glaciers have been stable or expanding in both test sites compared to the global retreat of mountain glaciers (Copland et al., 2011; Rankl et al., 2014; Bhambri et al., 2017; Steiner et al., 2018). Therefore, an automatic method is needed to rapid regularly update glacier inventories, while both test areas in our study were suitable for a comprehensive examination of the proposed method.

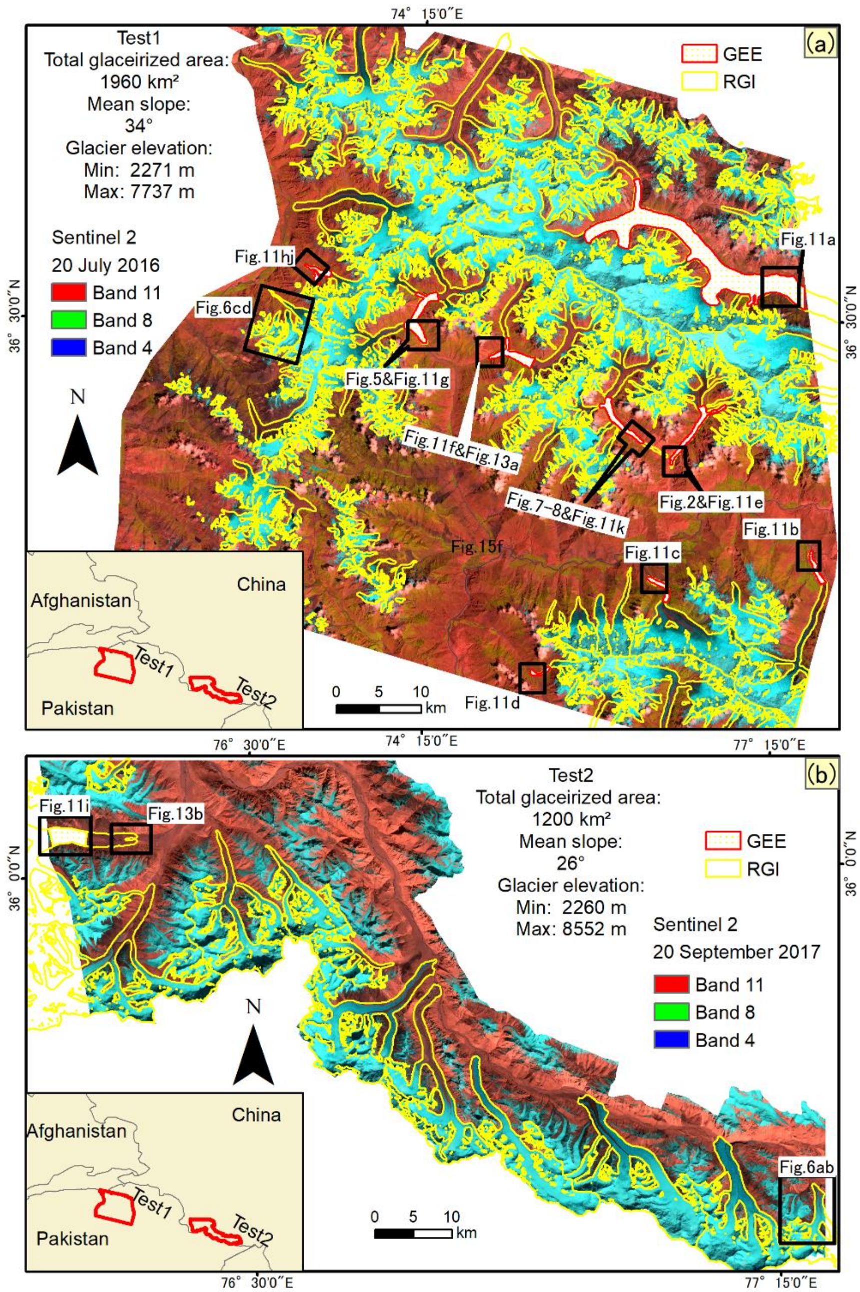

Fig. 1. The overall location of Test1 area (a) and Test2 area (b). (debris-covered ice outline (in red white-colored) is derived from the manual delineation of higher resolution Google Earth (GE)) images, glacier outline (in blue) is from Randolph Glacier Inventory (RGI).

2.2 Datasets

Optical imagery (radiometrically and geometrically corrected Sentinel-2A MSI Level-1C data), coherence images derived from two pairs of VV polarization SAR images (Sentinel-1A single- look complex format (SLC) Interferometric Wide Swath data), thermal imagery (Landsat 8 data, which contains the highest quality Level-1 Precision Terrain), and a digital elevation models (DEMs) (Advanced Land Observing Satellite (ALOS) World 3D 30 m mesh (AW3D30)) (Takaku et al., 2014; Liu et al., 2019) were used to map the debris-covered glaciers in this study (Table 1). Our rationale for using these datasets was:

- Optical images can help detect spectral differences between (debris-covered) glaciers and their surroundings,
- Thermal images can help detect radiometric temperature differences,
- SAR coherence images can help detect glacier motion,
- DEM-derived topographic characteristics such as mean slope can determine the general glacier boundary due to glacier almost formed on the gradual slope, while plan curvature and profile curvature can highlight convex and concave terrain allow for better detection of the glacier margin. AW3D30 was used as the DEM in this study because it reportedly has the higher accuracy over High Mountain Asia compared to other free available DEMs (Liu et al., 2019).

Recently, it was recognized that some glaciers rapidly advance (Rashid et al., 2020) within a short time in both test areas (Rankl et al., 2014; Bhambri et al., 2017; Steiner et al., 2018). Thus, the uncertainty of detected glacier termini as well as the map validation accuracy may be affected if glacier advances occurred between the acquisition dates of the different multisensor remote sensing data. Therefore, careful checking was done based on previous studies and visual comparison of the panchromatic band (15 m spatial resolution) of Landsat images and Sentinel-2 images. As a result, we found that almost no change or very small change occurred in the study area during 2016-2017 (Fig. 2).

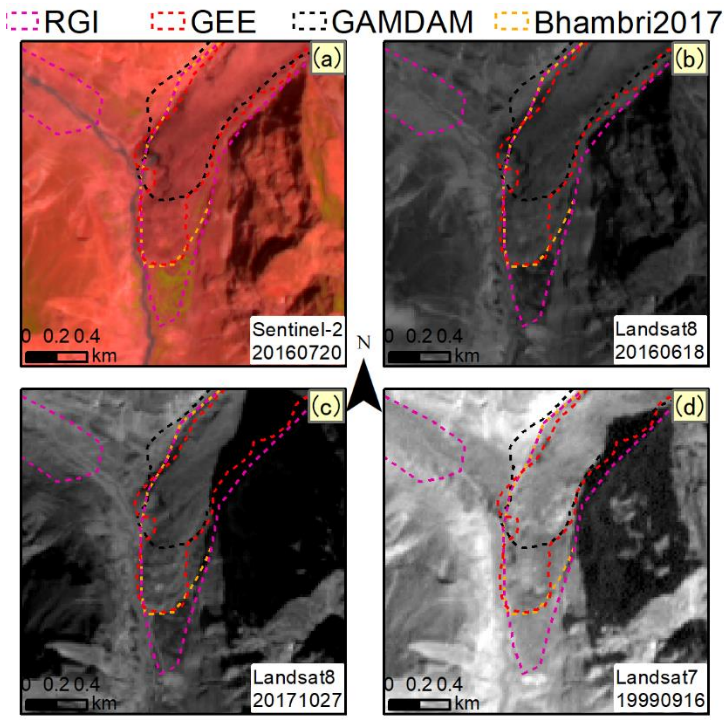

Fig. 2. Example of checking of Shishpar glacier surge activity.

Table 1
Data used for glacier mapping.

Data	Acquisition time (YearMonthDay)	Bands	Wavelength (μm)	Resolution (m)
Sentinel-1 (SLC)	Test1 20161124&20161224 Test2 20170928&20171127	C band IW mode	5.6 cm	2.3 x 14.1
Sentinel-2	Test1 20160720 Test2 20170920	VNIR (B2, B3, B4 & B8) NIR (B5, B6, B7 & B8a) SWIR (B11 & B12) VNIR (B1 & B9) – SWIR (B10)	0.55 – 0.90 0.70 – 0.88 1.57 – 2.28 0.43 – 1.40	10 20 20 60
Landsat 8	Test1 20160720 Test2 20171029	VNIR (B1, B2, B3 & B4)) SWIR (B6 & B7) PAN (B8) TIR (B10 & B11)	0.44 – 0.88 1.57 – 2.30 0.50 – 0.68 10.60 – 12.51	30 30 15 100
AW3D30	Both area 2006-2011	derived from optical images from ALOS		30

Two kinds of validation datasets were used for evaluating the results derived from this study. One is point vector data that were generated from the Randolph Glacier Inventory (RGI 6.0) (RGI Consortium, 2017) and S2 data (See methodology section). Other kinds of reference data are polygon vector data from RGI 6.0 (glacier outlines from RGI are taken from (Mölg et al., 2018)), previous study (Bhambri et al., 2017) and updated Glacier Area Mapping for Discharge from the Asian Mountains (GAMDAM) (Sakai, 2019) (Table 2). Additionally, debris-covered ice outlines were created using free available high-resolution Google Earth™ (GE) images by manual delineation (Table 2). Multi-temporal high resolution satellite images from different sources and a DEM provided by Google Earth™ (GE) allow the 3D view of glacier landscape which increased the differentiate the bumpy glacier surface and helpful for the generating accurate reference data by manual digitization of glacier outlines. To simplify the notation, RGI, Bhambri2017, GAMDAM and GE are referring to reference glacier outlies for the duration of the paper. Evaluating the accuracy of satellite-derived glacier outlines is usually difficult due to a lack of ground truth data. It is widely accepted that glacier areas mapped from medium resolution data (such as data used in this study) can be validated by glacier areas estimated from higher-resolution images due to the latter providing clear visibility of details of the surface. Thus, glacier area estimated from a higher-resolution images cloud be considered as 'ground-truth'. But, manual delineation of debris-covered glaciers can have relatively high uncertainty, even based on higher resolution images (Paul et al., 2013). In this regard, following the suggestion by Paul et al., 2013, glacier outlines from different sources of data like RGI, Bhambri2017, GAMDAM, and GE were used for performing a multiple digitization experiment based on the same a set of glaciers and then comparing their differences.

Table 2
Detailed information about reference datasets used in this study.

DC area No. (CF)	GAMDAM (Rm) DC area	RGI (Rm) DC area	Bhambri et al., 2017 (Rm) DC area	GE (IS&Rm) DC area
1 (Fig. 11a)	19970810 (30) 60.53 km²	19990916 (30) 60.80 km²	20131009 (30) 61.29 km²	20160619 (WorldView-2&1.8) 60.53 km²
2 (Fig. 11e)	19970810 (30) 3.37 km²	19990916 (30) 3.72 km²	20131009 (30) 3.71 km²	20160619 (WorldView-2&1.8) 3.49 km²
3 (Fig. 11g)	20010711 (30) 7.49 km²	19990916 (30) 7.13 km²	20150819 (30) 7.04 km²	20171009 (SPOT7&1.5) 7.21 km²
4 (Fig. 11k)	19970810 (30) 4.35 km²	19990916 (30) 5.11 km²	20131009 (30) 4.05 km²	20160619 (WorldView-2&1.8) 4.75 km²
5 (Fig. 11f)	19970810 (30) 4.79 km²	19990916 (30) 4.78 km²	20131009 (30) 4.82 km²	20171009 (Pléiades-1&2) 5.01 km²
6 (Fig. 11c)	19970810 (30) 0.67 km²	20010829 (30) 0.91 km²	20131009 (30) 0.91 km²	20160619 (WorldView-2&1.8) 0.72 km²
7 (Fig. 11b)	19970810 (30) 2.15 km²	20010829 (30) 2.00 km²	20131009 (30) 1.93 km²	20160619 (WorldView-2&1.8) 2.01 km²
8 (Fig. 11h)	20010711 (30) 1.62 km²	19990916 (30) 1.58 km²	Not available	20160619 (WorldView-2&1.8) 1.65 km²
9 (Fig. 11d)	19970810 (30) 0.83 km²	20010829 (30) 0.73 km²	Not available	20161109 (WorldView-3&1.2) 0.93 km²
10 (Fig. 11j)	20010711 (30) 0.34 km²	19990916 (30) 0.30 km²	Not available	20160619 (WorldView-2&1.8) 0.31 km²
11 (Fig. 11i)	19970810 (30) 9.27 km²	19990916 (30) 9.22 km²	20130714 9.36 km²	20170618 (Pléiades-1&2) 9.40 km²

Note: CF: corresponding figures; DC: debris-covered; (RM): resolution of data used, unit in meter; IS: image source

3. Machine learning classifiers

Machine learning classifiers (MLCs) can produce effective and efficient classification results from remotely sensed images (Maxwell et al., 2018). MLCs can process high dimensional data and are able to classified the target feature with very complicated signatures (Belgiu and Drăguţ, 2016; Maxwell et al., 2018). Several machine learning reviews have been produced and concluded the machine learning methods can give a higher classification accuracy in comparison with conventional parametric classifiers (Mountrakis et al., 2011; Li et al., 2014b; Maxwell et al., 2018). MLCs belong to the category of supervised learning, where the classification algorithms learn from a pre-defined set of "training examples" input given to it and then use this learning to classify new observations. The following MLCs have been tested in this study:

- K-nearest neighbors (KNN), a popular technique which uses kernel functions to weight the neighbors according to their distances. KNN classifies the data points based on the points that are most similar to it (Altman, 1992; Maselli et al., 2005). It considered as non-parametric because KNN makes no statistical assumption about the data. The model is made up entirely from the given data. However, it is an example of "lazy learning" because little training is involved when this method is used (Altman, 1992; Maselli et al., 2005). Moreover, two hyper-parameters have to be set: the number of nearest neighbors (k) and weight options are needed to set before training KNN.
- Support vector machine (SVM), an algorithm that mostly concentrates on the training data (called support vectors) that are nearest to the optimal boundary between the two classes (Pal, 2008; Mather and Tso, 2016; Maxwell et al., 2018). The SVM aims to detect the best possible hyperplane that can the greatest possible separability between the two classes. (Maxwell et al., 2018). Therefore, an SVM classifier inherently is good at binary classification. SVM requires the selecting of several parameters including the type of kernel (linear, polynomial and the Radial Basis Function (rbf)), values of the regularization parameter (C), and kernel specific parameters (e.g. the gamma value for the rbf kernel) (Mountrakis et al., 2011). The selecting of an appropriate kernel function directly influences SVM based classification results (Mather and Tso, 2016). Previous studies suggested that rbf and linear spline kernels performed well for land cover classification using multispectral datasets (Pal, 2002; Watanachaturaporn et al., 2008).

- Decision tree (DT), it makes a multistage decision with a tree-like model (Safavian and Landgrebe, 1991). It splits the observations into smaller subdivisions (leaves) based on the most significant predictor (rules are learned sequentially) from input training samples (Safavian and Landgrebe, 1991; Friedl and Brodley, 1997). Then, it will select the one that produces the highest accuracy, and repeat until it successfully splits the data in all leaves (or reaches the maximum depth) (Safavian and Landgrebe, 1991; Friedl and Brodley, 1997). The advantages of DT are its ease of interpretation, ability to perform well with limited training data, capacity to process both numerical and categorical data, and high speed (due to the absence of complex mathematical requirements) (Pal and Mather, 2003). It should be noted that the hyper-parameters (criterion, min samples split and max depth) values affect the predictive performance of the induced DT.
- Gradient boosting (GB), an ensemble algorithm that integrates the results of several subsampled base classifiers to improve the predictive performance compared to the individual base classifier (Opitz and Maclin, 1999; Lawrence et al., 2004). The principle idea behind GB is learning from the many weak learning base classifiers (residual error) to create a final strong predictive model. This technique minimizes error in data classification through iterative runs and decision trees. At each time, it adjusts new trees to improve the previous tree and continue self-adjustment to reduce mean-squared error (Zhang et al., 2015). Moreover, three parameters (learning rate, number of trees and subsample) values need to be defined in GB training.
- Random forest (RF) is another ensemble algorithm, which builds a large number of DTs, and merges the results of these DTs together to get a more accurate and stable prediction compared to a single DT (Breiman, 2001). For each DT, a random subset of the training sample and a random subset of the classification features are used (Breiman, 2001). Each tree casts a unit vote and the class that receives the greatest number of votes is selected as the final predicted class (Breiman, 2001). This process improves the predictive accuracy of the model and controls over-fitting by integrating a many subsampled trees to reducing the variance. To train an RF model, hyper-

parameters like ‘max_features’ which is the maximum number of randomly selected features used for best split and ‘n_estimators’ which is the number of trees in the RF model are need to be set.

- Multi-layer perceptron (MLP) is a feedforward artificial neural network (ANN) model that has been found suitable for remote sensing classification problems (Foody, 2004; Yuan et al., 2009). MLP is composed of several layers. The first layer is named as the input layer. In this layer, input values are distributed to all units in the next layer (Rumelhart et al., 1985). The last layer is called the output layer which outputs the classification results (Rumelhart et al., 1985). Layer between the above-mentioned layers is known as the hidden layer (Rumelhart et al., 1985). MLP builds many simple units and, name as neurons or perceptrons. Each of the neurons can make simple decisions based on the learning of training samples. Then, neuron feeds those decisions to other neurons (based on activation function) by organized interconnected layers to generate final predictions. For training the MLP, parameters like the number of hidden layers, activation function, learning rate, alpha, and the number of iterations need to be defined.

4. Methodology

This section introduces the proposed automatic classification schemes for the hierarchical mapping of glaciers using the machine learning classifiers. The automatic classification scheme consists of several steps: pre-processing, generating an initial debris-free ice map, generating the training data set, implementation of MLCs and accuracy assessment (Fig. 3).

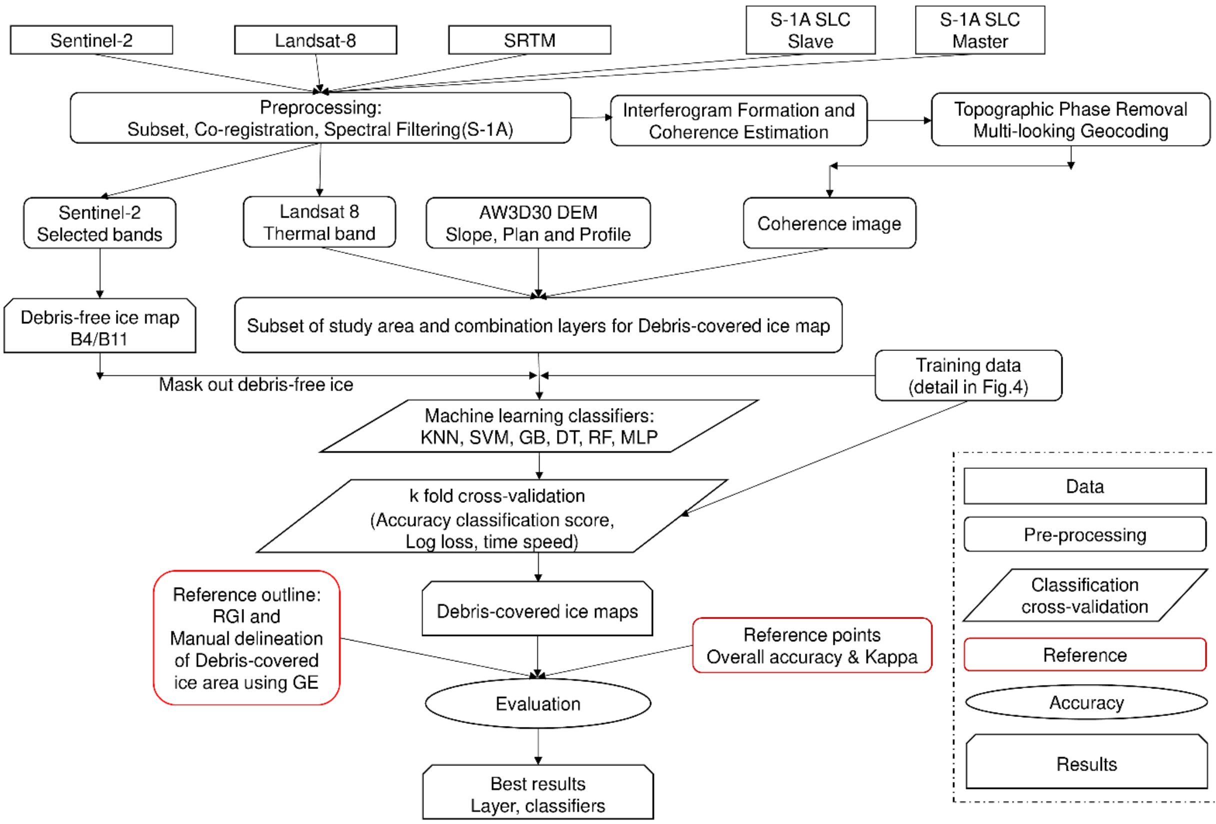

Fig. 3. Proposed flowchart of methodology for this study.

4.1 Pre-processing

1) Resampling: Sentinel-2 images were resampled to 30 m resolution which is the same resolution with Landsat 8 images and the DEM using a bilinear interpolation method.

2) Co-registration: Sentinel-2 images are co-registered with Landsat 8 images using ground control points (GCPs) collected from the same location in both images that are clear visible and considerably stable points. The co-registration error was controlled at less than 0.4 pixels.

3) SAR Coherence processing: a pair of Sentinel-1 images were processed to generate the SAR Coherence data. VV polarized SLC S1 images were combined with interferometric processing (TOPSAR co-registration interferogram IW all Swaths using SRTM, Multilooking, Speckle filer, Range Doppler terrain correction) using the freely available sentinel toolbox software (Veci et al., 2014). This step can be done automatically by using the Sentinel Toolbox Graph Builder.

4) Extraction of the geomorphometric parameters (GMPs): GMPs were extracted from AW3D30 DEM.

5) Subsetting the data: all images (S2, Coherence, TIR, and GMPs) were subset to the study area boundary.

6) Generation of raster layers: Finally, several raster layers that contain the different raster combinations (Table 3) were generated to test the band sensitivity and accuracy performance. Green (b3), Red (b4), NIR (b8&b8a) and SWIR (b11&b12) bands of S2 were selected due to they can enhance differentiability of debris-covered ice from surrounding rocky materials (Table 3).

Table 3
Selection of raster bands for different raster layers.

Raster	Optical-SAR-TIR-GMP	Optical-SAR-GMP	Optical-SAR-TIR	Optical-TIR-GMP
Coherence image S1A	☑	☑	☑	☒
Thermal L8	☑	☒	☑	☑
Sb11/Sb12	☑	☑	☑	☑
Plan curvature DEM	☑	☑	☒	☑
Profile curvature DEM	☑	☑	☒	☑
Slope DEM	☑	☑	☒	☑
S2 b11	☑	☑	☑	☑
S2 b8	☑	☑	☑	☑
S2 b4	☑	☑	☑	☑
S2 b3	☑	☑	☑	☑
S2 b8a	☑	☑	☑	☑

4.2 Debris-free ice map

Automated mapping techniques of the debris-free ice were developed based on the fact that snow and ice have high reflectivity in the visible to VNIR wavelengths. On the other hand, snow and ice have a very low reflectivity in the SWIR wavelength region. The band ratio method is based on this property and is known to be as accurate and robust (Racoviteanu et al., 2009; Paul et al., 2013). Therefore, in this study, the map of debris-free ice was generated using the conventional band ratio method (S2b4(Red)/S2b11(SWIR) ≥1.8) (Paul et al., 2016).

4.3 Generating the training data sets

The generation of accurate training data is crucial to the accuracy of classification results. However, accurate training data are extensively based on human knowledge. Manual selection of samples is time-consuming. Therefore, a new idea was presented here for automatically generating the training data accurately and this was achieved by creating zones that exclude the uncertain glacier margins. First, we found that existing glacier outlines from RGI (Fig. 4 and 5a) were generated using Landsat images around 1999/2000. Therefore, visually checking was done based on S2 false-color composite images whether large area difference existed in the glacier tongue. Then, for generating training data, two relatively stable boundary layers: debris-covered ice area and non-glacier area, were created (Fig. 4a, Fig. 5e and d) by applying buffers to existing RGI outlines (Fig. 4). In the case of debris-covered ice areas (Fig. 5d, yellow-colored boundary), we applied an internal buffer (buffer distance = -200 m) to the RGI debris-covered glacier ice boundary (RGI outlines clip the debris-free ice map). On the other hand, the non-glacier area (Fig. 5e, cyan colored boundary) was derived from the intersecting of two different external buffer zones (areas located between the 100m and 1000m buffers) of RGI outlines. Finally, randomly placed training points (2,000 and 20,000 points for Test1 area, 20,000 points for Test2 area) were generated in both Test1/Test2 areas, and points were assigned to the "non-glacier" or "debris-covered ice" class based on debris-covered layer and non-glacier layer (Fig. 4 and 5f). In addition, these threshold values may also apply other regions but visual checking is needed to judge whether large area changes existed between the RGI and investigated period.

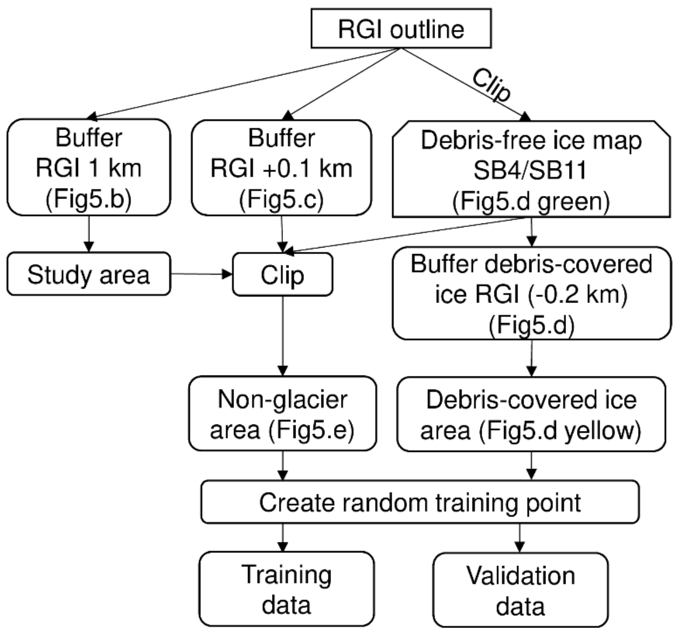

Fig. 4. Methodology flowchart for automated training points generation.

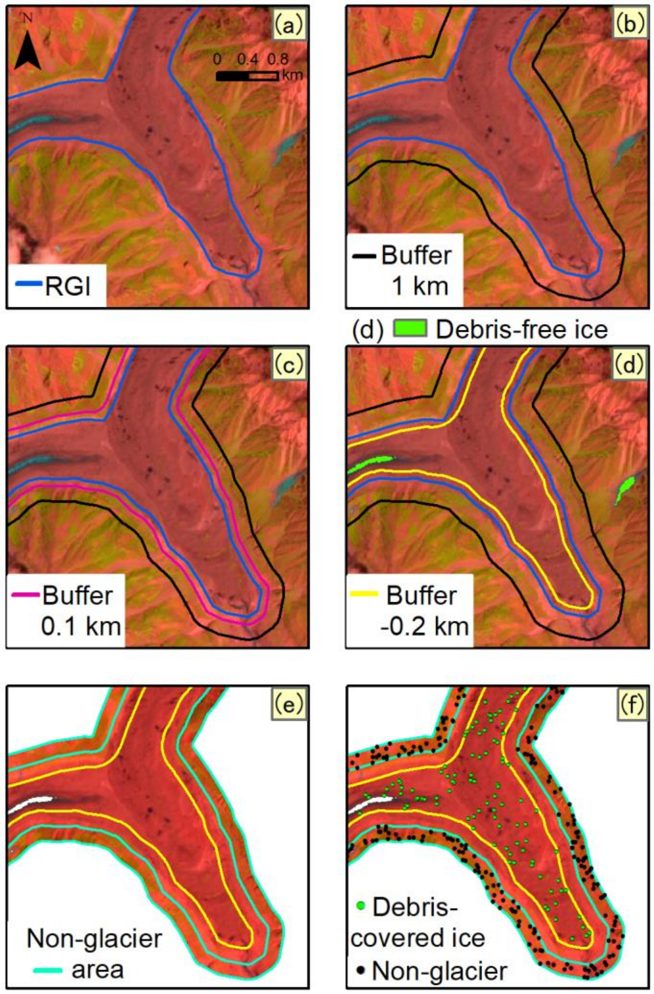

Fig. 5. Example of automated training points generation.

4.4 Implementation of MLCs for mapping of debris-covered ice

Prior to classification, to mask out a large number of high similarity pixels (spectral/thermal) from the combination raster layers and reduce the processing time, a vector layer generated from a one km buffer of the RGI (Fig. 5b) and debris-free ice maps were used. As an initial step, the performance of all machine learning classifiers was compared based on the accuracy of the debris-covered ice maps derived from the Test1 area using the smaller set of training points (2,000). Then, to evaluate the transferability of the method, the top three classifiers (from the previous step) were used for classifying debris-covered ice in both Test1 and Test2 areas using all 20,000 training points.

Next, MLC models in the open-source "scikit-learn" package were implemented in this study (Pedregosa et al., 2011). All MLCs were conducted in a Python environment on an Intel(R) Core (TM) CPU i7-6700 @3.41 GHz processor with 8.00 GB memory (RAM). In general, learning algorithms benefit from data set standardization, because normalized/standardized processing can improve the numerical condition of the optimization problem (Sarle, 2002). Therefore, before performing the MLCs, all input features were normalized/standardized. To optimize the hyper-parameters of the MLCs (Table 4), the training data were divided into training (80% of the training data) and evaluation (20% of the training data) subsets, and a grid-search (based on 10-folds cross-validation) was used to identify the best hyper-parameters that produced the highest classification results. The search range for each of the hyper-parameter values was based on literature review (Table 4) (Hsu et al., 2003; Kavzoglu and Mather, 2003; Haapanen et al., 2004; Pal, 2005; Elith et al., 2008; Li et al., 2014a; Qian et al., 2015; Pham et al., 2017; Thanh Noi and Kappas, 2018; Yang et al., 2019). However, wider ranges compared to the literature were defined in this study. Finally, the hyper-parameters that were found to produce the highest cross-validation accuracy were used to perform the final training of MLC models (i.e. using all of the training data). To compare all MLCs, the final classification results were first evaluated by classification metrics such as accuracy_score, log_loss, and overall accuracy. The accuracy_score, log_loss was estimated based on evaluation (20% of training data) subsets. Log loss calculated the uncertainty of the MLCs prediction using the predicted result compared to evaluation subsets (Nielsen, 2015). This gave a more nuanced view about the accuracy of the model because the goal of MLCs is to minimize this value (Nielsen, 2015).

Table 4
Optimizing of various hyper-parameters for machine learning classifiers (MLCs).

MLCs	Grid search Hyper-parameters value	Reference
KNN	Number of neighbors = 1 to 30 weight option = uniform, distance	Qian et al. 2015; Haapanen et al. 2004
SVM_linear	C = logspace(-3, 2, 6)	Hsu et al. 2003; Li et al. 2014a
SVM_rbf	Gamma = 2.0**sp.arange(-15,4,2) C = 2.0**sp.arange(-5,16,2)	Hsu et al. 2003; Li et al. 2014a
GB	learning_rate = [1, 0.5, 0.25, 0.1, 0.05, 0.01], n_estimators = [1, 2, 4, 8, 16, 32, 64, 100, 200,1000]	Elith et al. 2008; Yang et al. 2019
DC	Criterion (C) = gini, entropy, min_samples_split = range (10, 500, 20), max_depth = [1, 3, 5, 7, 9, 11, 13, 15, 17, 19]	Elith et al. 2008; Li et al. 2014a
RF	n_estimators = sp.arange(100,1100,100), max_features = auto, criterion= gini	Thanh Noi and Kappas 2018; Pal 2005; Elith et al. 2008; Li et al. 2014a
MLP	Solver (S) = 'lbfgs', max_iter = [1000], alpha (A) = 10.0 ** -np.arange(1, 10), hidden_layer_sizes = np.arange(4, 28, 4)	Pham et al. 2017; Kavzoglu and Mather 2003

4.5 Accuracy assessment

On one hand, overall accuracy was estimated based on 500 random vector points per class. These points were randomly generated based on RGI and then manually checked using S1 and Google earth images. Overall accuracy, kappa coefficient of overall and each classes were calculated along with their variances. On the other hand, for a comprehensive analysis of classification method effort, reference polygons (11 selected debris-covered ice areas) were manually digitized using higher resolution GE images and extracted at the same digitized area from reference polygons. Selection of these 11 reference polygons was due to them having debris-covered ice with differences in size, debris condition (partly or fully covered by debris), and aspect (direction of glacier termini). Importantly, in these selected digitized areas, there were high-resolution Google Earth images with a close temporal acquisition date to the satellite data used for classification and minimum snow cover condition, allowing for the generation of high quality reference data. Finally, the area difference between results (based on Optical-SAR-TIR-GMP classification) derived from this study and references was calculated for the evaluation of the mapping accuracy. The percentage of area difference was calculated as the area difference between mapped area and reference area, dividing by reference area and multiplying the result by 100.

5. Results

Fig. 6 shows the results of the debris-free glaciers of Test1 and Test2. The initial debris-free ice map generated using the band ratio approach showed a high similarity with S2 false-color composite images and SAR coherence images (Fig. 6). Previous studies have already concluded that debris-free ice can be mapped with high accuracy using simple band ratio methods, e.g. using the Red/NIR band ratio image of Landsat data or S2 data (Racoviteanu et al., 2009; Paul et al., 2016). Therefore, the debris-free ice map derived from this study was not discussed in detail. Next, specific details on the classification results of debris-covered ice derived from different training samples and tuning parameters for the MLCs are described in the following paragraph.

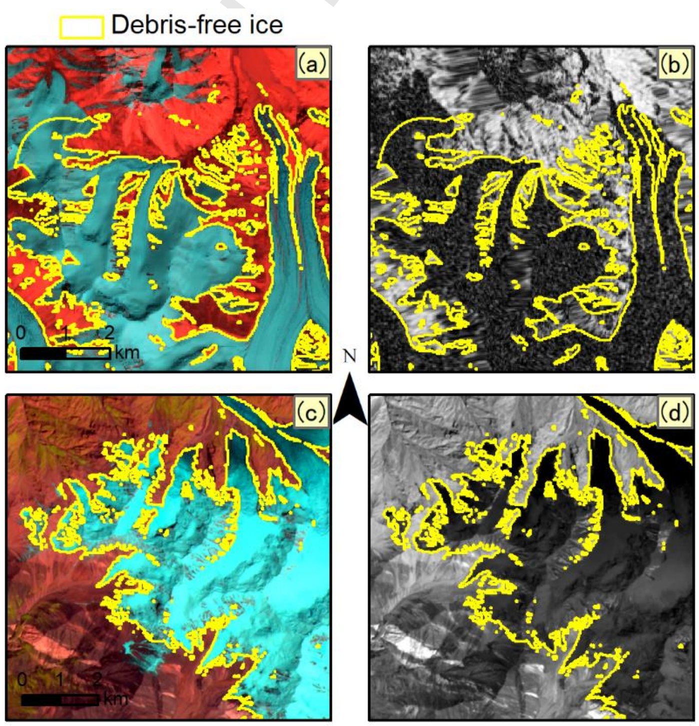

Fig. 6. Example of results of debris-free glacier maps of Test1 (a&b) and Test2 (c&d) showed the remarkable similarity with overlaid false-colour Sentinel-2 (a&c) and Sentinel-1 coherence images (b&d). The debris-free glacier can easily distinguish from a stable mountain area based on spectral difference and loss of coherence (dark shaded area).

5.1 Comparisons of debris-covered ice maps derived from MCLs based on different layers and 2000 training samples in Test1 area

Generally, the visual comparison and accuracy score indicated that results derived from most of all MLCs based on the Optical-SAR-TIR-GMP layer have higher accuracy compared to the results from other layer combinations (Fig. 7 and 9). This is likely due to the MLC classifiers were able to extract useful classification features from all of the multi-sensor data (i.e. the optical, SAR, thermal, and GMP). The second highest accuracy was obtained from results derived from MLCs based on the Optical-SAR-GMP layer and then followed by Optical-TIR-GMP and Optical-SAR-TIR layers. Particularly, the best results were derived from the Optical-SAR-TIR-GMP layer due to the lowest misclassification rate of both the debris-covered ice area and the non-glacier area near the glacier tongue (Fig. 7 and 9). For example, various degree of underestimation of debris-covered ice area in the glacier tongue occurred in results derived from Optical-SAR-TIR layer (Fig. 7e1-e4 and Fig. 8e1-e3). Results derived from Optical-SAR-GMP (Fig. 7d1-d4 and Fig. 8d1-d3) and Optical-TIR-GMP layers (Fig. 7f1-f4 and Fig. 8f1-f3) indicated that different levels of the non-glacier area near the glacier tongue were misclassified as debris-covered ice. All results derived from MLCs based on different combinations of raster layers contained some isolated pixels (shown in Fig. 7 and 8 in blue color). These isolated pixels were removed automatically using the procedure presented in Section 5.2. According to visual comparison and accuracy scores, the Optical-SAR-TIR-DEM combined layer always produced the highest accuracy, and therefore, it was selected to evaluate the performance of MLCs (presented in the next section).

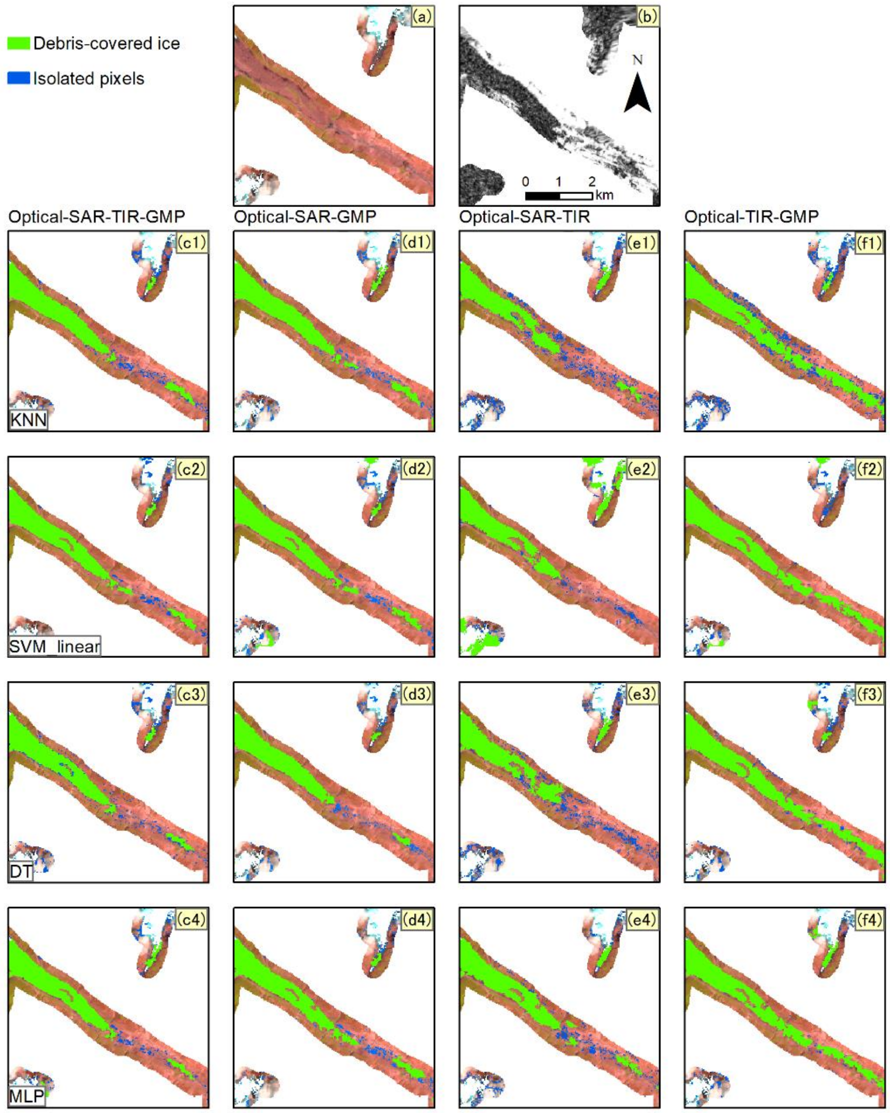

Fig. 7. Debris-covered ice maps of Test1 area obtained from KNN, SVM_linear, DT, and MLP classifiers based on different layers and 2000 training points. All figures present the same location of (a) False-colour Sentinel-2 images and (b) Sentinel-1 coherence images. Classification results obtained from Optical-SAR-TIR-GMP layer showed the better differentiation of debris-covered ice from surrounding areas, then followed by Optical-SAR-GMP, Optical-SAR-TIR, and Optical-TIR-GMP.

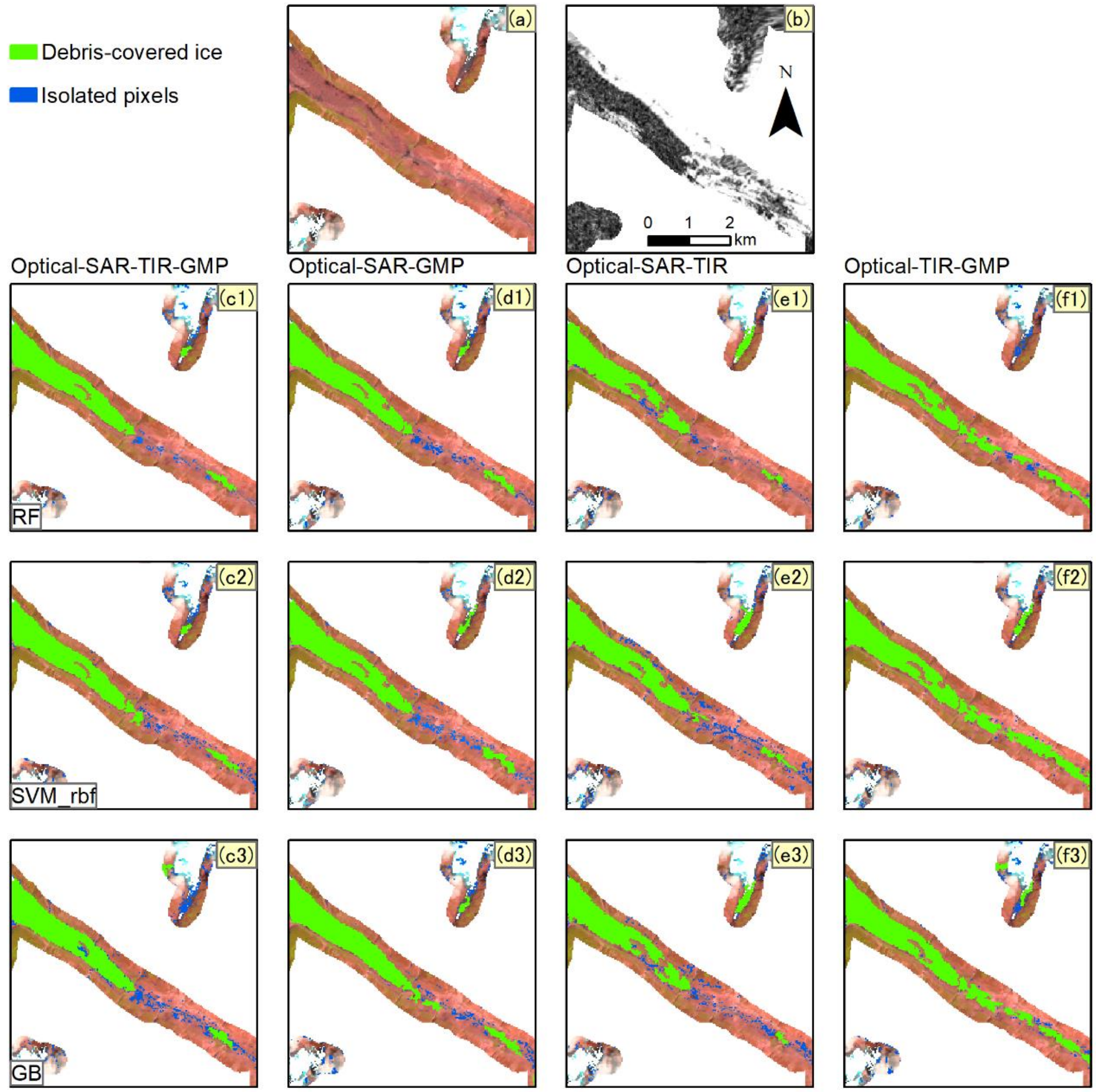

Fig. 8. Debris-covered ice maps of Test1 area obtained from RF, SVM_rbfa and GB classifiers based on different layers and 2000 training points. All figures present the same location of (a) False-colour Sentinel-2 images and (b) Sentinel-1 coherence images. Classification results obtained from Optical-SAR-TIR-GMP layer showed the better differentiation of debris-covered ice from surrounding areas, then followed by Optical-SAR-GMP, Optical-SAR-TIR, and Optical-TIR-GMP.

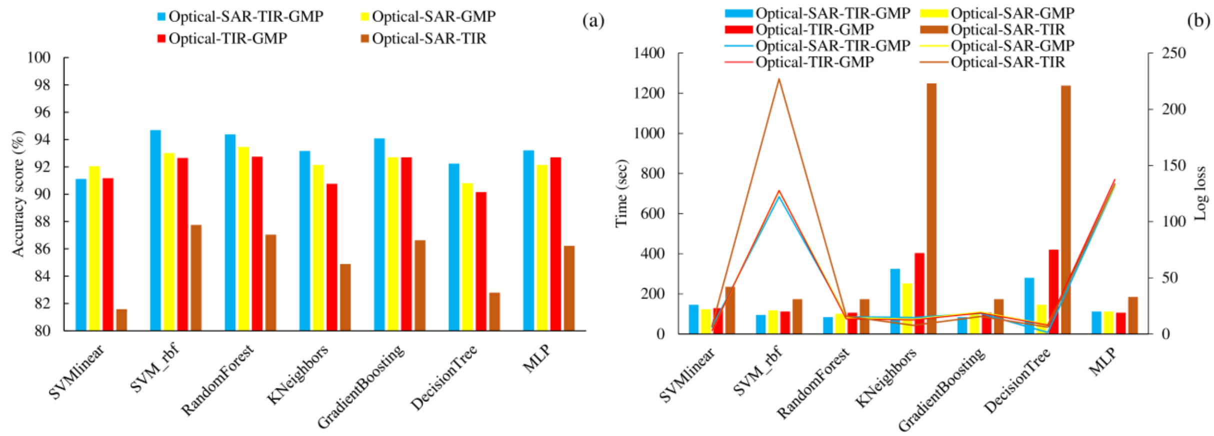

Fig. 9. Accuracy score (a), log loss (b), and classification speed (colored line in (b)) estimated from machine learning classifiers based on four different layers and 2000 training points. Classification results from Optical-SAR-TIR-GMP layer illustrated the better accuracy than other layers. RF, GB, and SVM_rbf classifiers were produced the highest accuracy score and lowest log loss.

5.2 Comparisons of debris-covered ice maps derived by MCLs based on Optical-SAR-TIR-GMP

The debris-covered ice maps produced by MLCs were evaluated based on visual comparison and a quantitative accuracy assessment. The comprehensive comparison of classification results (Fig. 7c1-c4, Fig. 8c1-c3, Fig. 9 and 10) derived from all MLCs indicated that RF, GB, and SVM_rbf were the most accurate classifiers (in that order), followed by MLP, KNN, DT, and SVM_linear (Fig. 9 and 10).

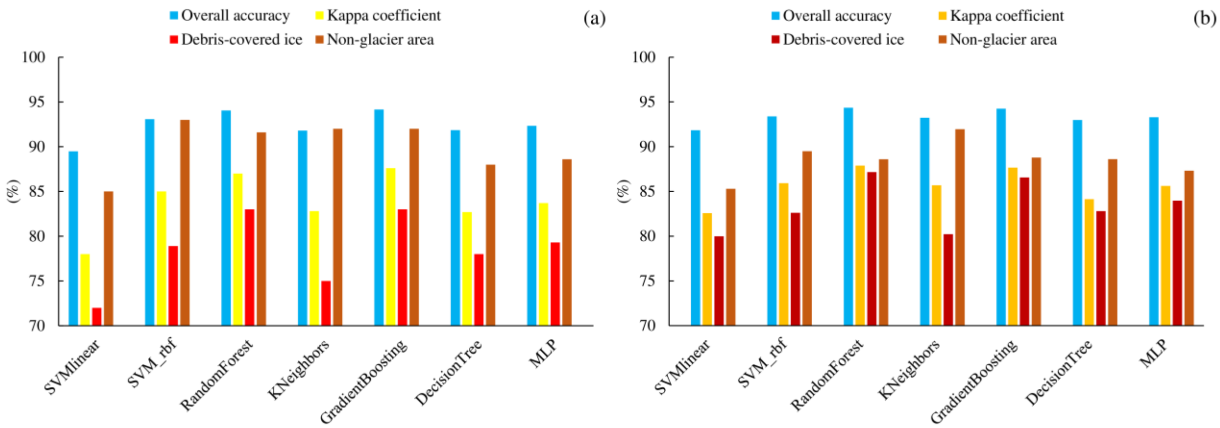

Fig. 10. Accuracy assessment of results before (a) and after (b) removed the isolated pixels derived from machine learning classifiers based on Optical-SAR-TIR-GMP and 2000 training samples. RF presented the best overall accuracy and kappa coefficient then followed by GB and SVM_rbf.

Varying degrees of the isolated pixels were existing in the results derived from the MLCs (Fig. 7c1-c4, Fig. 8c1-c3) because these pixels had higher similarity in spectral, thermal, and motion of the debris-covered ice with rock materials. However, these noisy isolated pixels can be easily removed (here, areas mapped as debris-covered ice that were less than 40 pixels in size were removed). The accuracy assessment indicated that the accuracy of debris-covered ice maps improved by 2-3 % when isolated pixels were removed. In the meantime, the order of performance of the MLCs remained unchanged such as RF, GB, and SVM_rbf respectively.

To investigate the relationship between the number of training points and classification accuracy as well as comparison of RF, GB and SVM_rbf classifiers performance and transferability of the method, debris-covered ice in Test1/Test2 were mapped using RF, GB and SVM_rbf classifiers based on Optical-SAR-TIR-GMP with 20,000 training points. Results derived from this larger number of training samples revealed that RF achieved higher accuracy than GB and SVM_rbf (Fig. 11). The accuracy of the debris-covered ice map was increased by 1-2% by increasing training points from 2,000 to 20,000 (Fig. 10 and 11). Additionally, the accuracy of debris-covered ice maps was improved by 0.5-1.5% when isolated pixels were removed (Fig. 10 and 11). The similar performance of RF using the small and large training sets is consistent with past research that found RF could achieve accurate classifications with limited training samples (Johnson and Xie, 2013).

Maps of debris-covered ice were converted to vector polygons for visual and estimated areal comparison with two reference datasets: One generated by manual delineation of part of the debris-covered ice using higher resolution Google Earth (GE) images, and another covering the same part of the debris-covered ice outline from RGI, GAMDAM and Bhambri2017 (Table 2, Fig. 12 and 13). Visual comparisons of debris-covered ice maps indicated that polygons derived from RF, GB, SVM_rbf were similar to the GE-derived polygons (date of the images used in GE are available in Table 2) in most of the debris-covered ice sites (i.e.: Fig. 12a, d, g, I, and j). The boundary of debris-covered ice derived from RF, GB, SVM_rbf has an obvious difference with polygon outlines from RGI, which are shown in Fig. 12e and k. Visual comparison of glacier outlines also revealed that the GB classifier mostly misclassified the small river which was connected to the glacier tongue (Fig. 12c).

Area differences between debris-covered ice derived from RF, GB, SVM_rbf classifiers (based on Optical-SAR-TIR-GMP using 20,000 training data) and reference polygons showed that smaller area differences were estimated between MLC classifiers and Bhambri2017&GE compared to area differences between the MLC classifiers and RGI&GAMDAM datasets (Fig. 13). Specifically, the debris-covered ice area derived from RF had the smallest area difference (average difference) compared to the reference datasets (Fig. 13). The areal and visual comparison both showed the RGI and GAMDAM in selected debris-covered ice sites had a much worse match with the results from this study due to the time mismatch of data acquisition used in RGI and GAMDAM (i.e.: Fig. 12e and k). On the contrary, the debris-covered ice areas derived from GB and SVM_rbf showed a very similar area difference compared to the reference area.

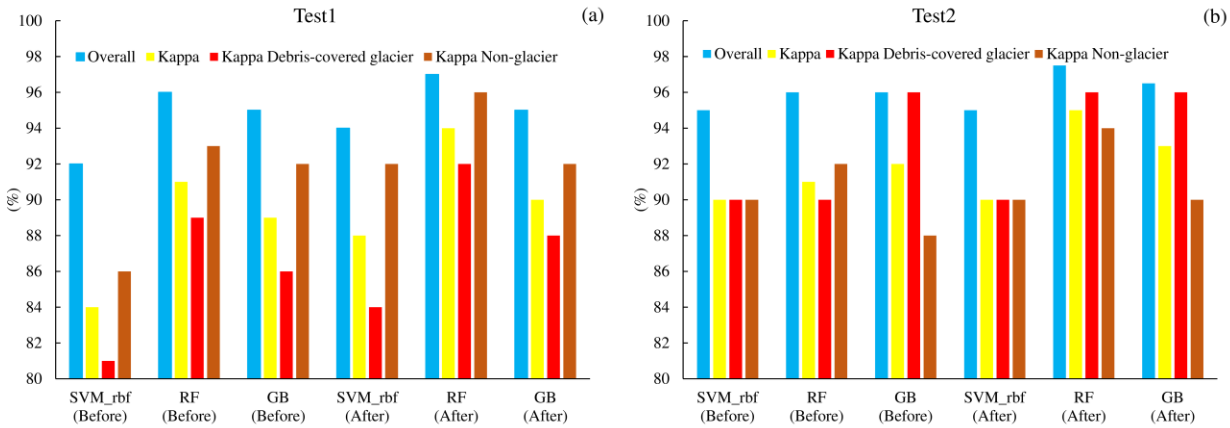

Fig. 11. Accuracy assessment of debris-covered ice maps ((a)Test1 and (b) Test2) before and after removing the isolated pixels derived RF, GB, and SVM_rbf classifiers based on Optical-SAR-TIR-GMP and 20000 training data. RF presented the best overall accuracy and kappa coefficient and classification accuracies were improved after isolated pixels were removed.

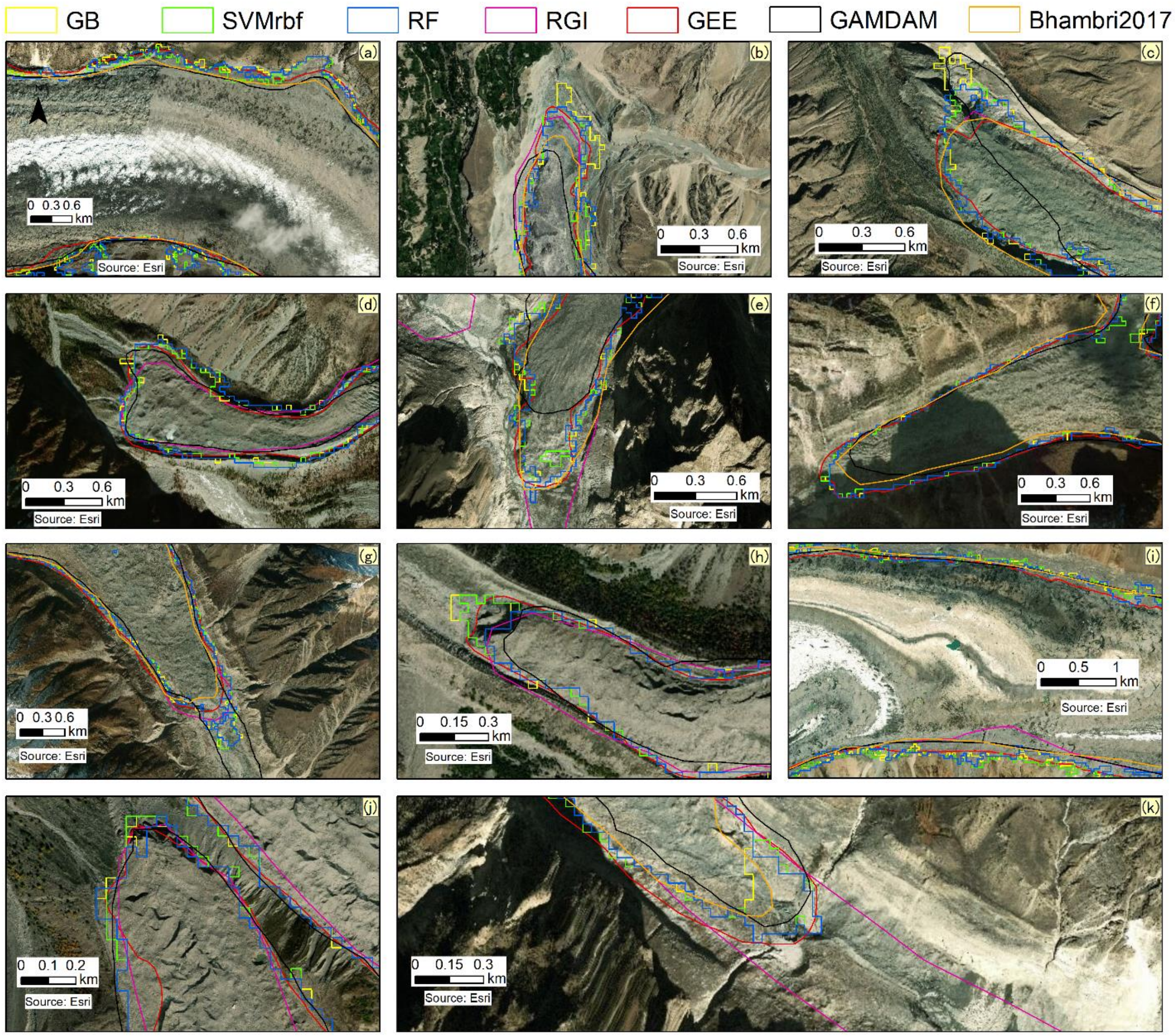

Fig. 12. Visual comparisons of debris-covered ice outlines derived from RF, GB, and SVM_rbf classifiers based on Optical-SAR-TIR-GMP using 20000 training points and reference polygons from the manual delineation of higher resolution GE images, RGI, GAMDAM, Bhambri2017. Most of the debris-covered outlines derived from RF, GB, and SVM_rbf were similar to the GE-derived polygons due to closed dates of the images (see Table 2) used for glacier mapping.

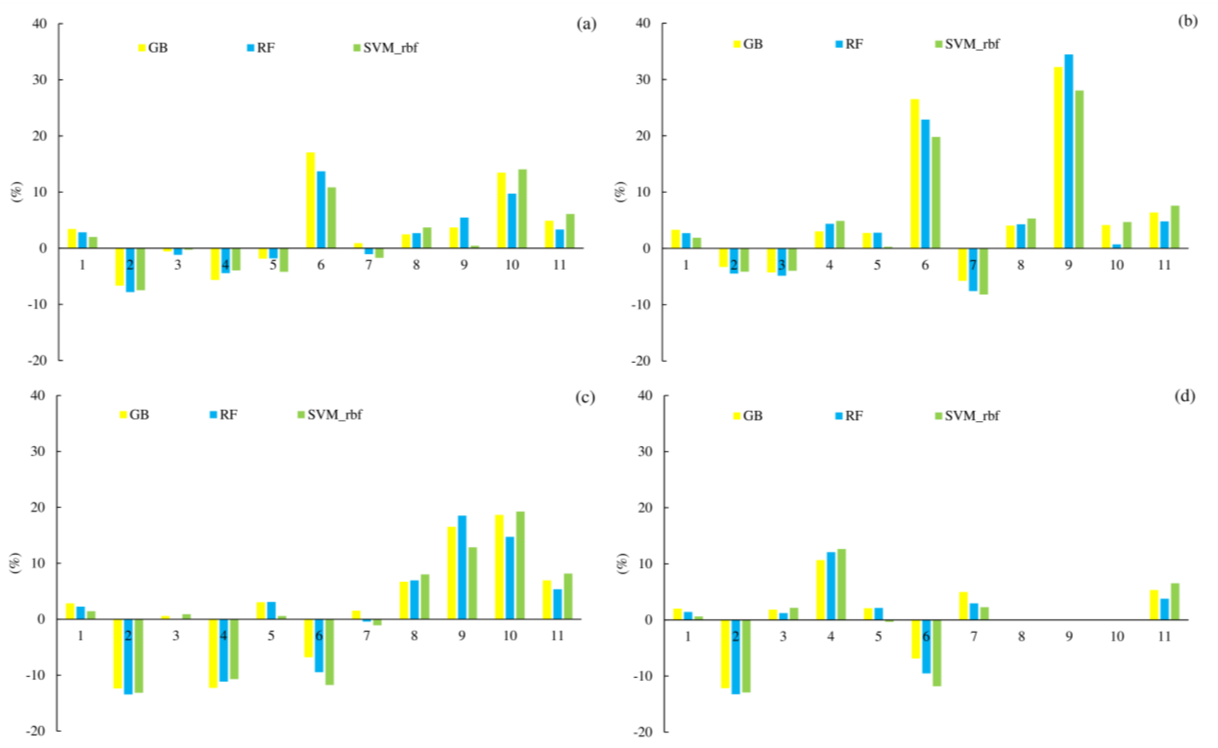

Fig. 13. Areal differences of debris-covered ice maps derived from RF, GB and SVM_rbf classifiers based on Optical-SAR-TIR-GMP and 20000 training points and reference polygons based on GE (a), GAMDAM (b) RGI (c), and, Bhambri et al., 2017 (d). RF had the smallest average area difference compared to the reference datasets.

5.3 MLCs parameters tuning

The optimal MLCs parameters and classification accuracy were calculated based on cross-validation, and are shown in Fig. 9 and 11 and Table 5. Fig. 9 and 11 illustrated that most of the highest accuracy of all MLCs were achieved based on Optical-SAR-TIR-DEM. Particularly, for KNN classifiers, the best classification accuracy was derived from the number of neighbors' value of 6 and distance weight function based on Optical-SAR-TIR-GMP (Table 5). For the SVM_linear classifier, the greatest classification accuracy was captured with a C value of 1 based on the Optical-SAR-GMP (Table 5). In the case of DT classifiers, the highest classification accuracy was acquired with a maximum depth value of 7 based on Optical-SAR-TIR-GMP (Table 5). Regarding MLP classifiers, the most reliable classification accuracy was achieved by the alpha value of 0.00001 and hidden layer sizes of 20 based on Optical-SAR-TIR-GMP

(Table 5). For SVM_rbf classifiers, classification accuracy (based on Optical-SAR-TIR-GMP and 20,000 training samples in both test areas) was the highest when a gamma value of 0.5 and a C value of 8 and 2 were selected (Fig. 11 and Table 5). In the case of GB classifiers, a learning rate value of 0.1 and a number of estimator's value of 1,000 derived the highest classification accuracy in the case of both test areas based on Optical-SAR-TIR-DEM and 20,000 training samples (Fig. 11 and Table 5). The highest classification accuracy was achieved for RF classifiers by a number of estimators values of 200 (for Test1) and 300 (for Test2) based on Optical-SAR-TIR-GMP and 20,000 training samples (Fig. 11). SVM_rbf and MPL classifiers have longer hyper-parameter tuning speed compared to other MLCs. Furthermore, RF and GB classifiers showed a more accurate and faster prediction model compared to other MLCs (Fig. 9 and Fig. 10 and 11).

Table 5
Best estimated hyper-parameters value for machine learning classifiers.

MLCs	Test1 TD2000 OSG	Test1 TD2000 OST	Test1 TD 2000 OTG	Test1 TD 2000 OSTG	Test1 TD 20000 OSTG	Test2 TD 20000 OSTG
KNN	NN = 12 WO = Distance	NN = 3 WO = Distance	NN = 6 WO = Distance	NN = 6 WO = Distance		
SVM_linear	C= 1	C = 10	C = 0.1	C = 10		
SVM_rbf	G = 0.5 C = 2	G = 0.03125 C = 8192	G = 0.03125 C = 512	G = 0.5 C = 8	G = 0.5 C = 8	G = 0.5 C = 2
GB	LR = 0.1 NE = 200	LR = 0.05 NE = 1000	LR = 0.1 NE = 1000	LR = 0.05 NE = 1000	LR = 0.1 NE = 1000	LR = 0.1 NE = 1000
DC	C = gini MSS = 10 MD = 5	C= gini MSS = 10 MD = 11	C = gini MSS = 10 MD = 7	C= gini MSS = 10 MD = 7		
RF	NE=500 MF=auto	NE=700 MF=auto	NE = 100 MF = auto	NE = 200 MF = auto	NE = 200 MF = auto	NE = 300 MF = auto
MLP	S = lbfgs A = 1e-09 HLS = 8	S = lbfgs A = 0.01 HLS = 20	S = lbfgs A = 1e-08 HLS = 8	S= lbfgs A = 1e-05 HLS = 20		

Note: Training data: TD; Optical-SAR-GMP: OSG; Optical-SAR-TIR: OST, Optical-TIR-GMP: OTG; Optical-SAR-TIR-GMP: OSTG; NN: Number of neighbors, WO: weight option, G: gamma, LR: learning rate, NE: n_estimators, MSS: min_samples_split, MD: max_depth, MF: max_features, S: Solver, A: alpha, HLS: hidden_layer_sizes

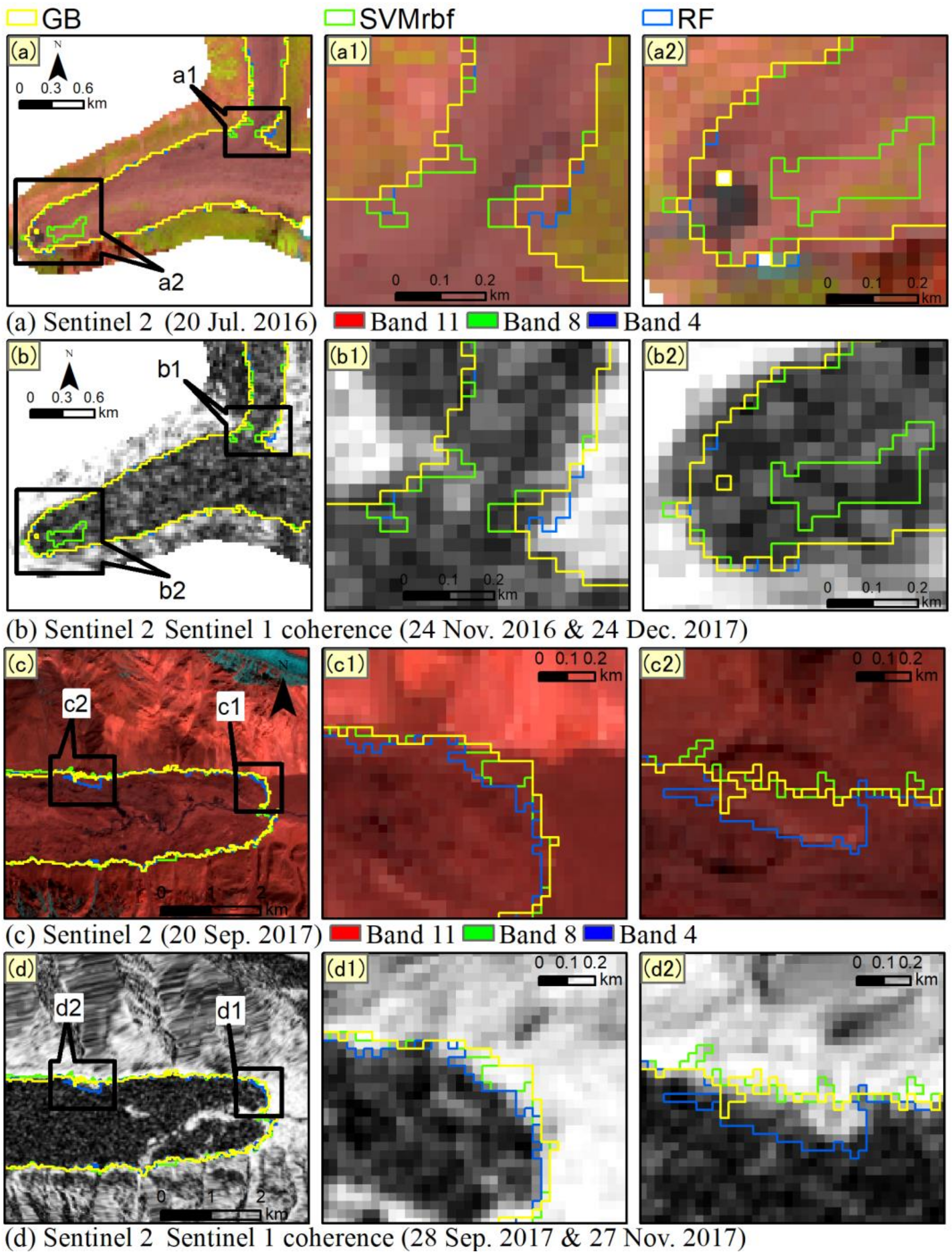

Fig. 14. Visual comparisons of debris-covered ice maps derived from the RF, GB and SVM_rbf classifiers based on Optical-SAR-TIR-GMP and 20000 training data in Test1 (a-b) and Test2 (c-d). RF classifiers better detecting the ice under the debris layer compared to GB and SVN_rbf.

6. Discussion

6.1 Comparisons of debris-covered ice maps based on different layers

As expected, visual comparison (Fig. 7 and 8) and accuracy scores (Fig. 9 and 10) of the classification results -derived from all MLCs and using different layer combinations - indicated that most of the MLCs achieved their highest accuracies based on the Optical-SAR-TIR-GMP combined layer. It further confirmed the conclusions (the combination of coherence, spectral, thermal and GMPs would helpful for accurate detection of debris-covered ice) of previous studies that multi-sensor data fusion is desirable for debris-covered glacier classification. However, it is important to consider which types of multi-sensor data to include for this mapping. For example, we found that classification accuracy using the Optical-SAR-TIR layers (without GMPs) was lower than that of other classifications that did not include one of these layers. This demonstrates that GMPs play a critical role in the accurate detection of debris-covered ice that cannot be overcome simply by using other types of multi-sensor (non-elevation) data. Furthermore, the classification accuracy of results derived from Optical-SAR-GMP and Optical-TIR-GMP layers illustrated that additional information from coherence and thermal images are helpful to increase the accuracy of debris-covers ice mapping. Importantly, use of the coherence image resulted in a greater increase in accuracy than use of the thermal infrared images, probably because of the coarser resolution (120 m) of the thermal data and the thicker debris on the glacier surface (which caused small difference in radiometric temperature between debris-covered ice and surrounding rocky materials).

6.2 Comparisons of debris-covered ice maps derived from MLCs based on Optical-SAR-TIR-GMP

Based on accuracy assessments (Fig. 9 and 11) and visual comparisons (Fig. 7c1-c4, Fig. 8c1-c3, and Fig. 12) of MLCs, the difference in accuracy between best three classifiers (RF GB and SVM_rbf) was relatively small. However, detailed comparison of the debris-covered ice outlines with coherence images showed that more accurate debris-covered ice areas were extracted by the RF classifiers (Fig. 14). On the other hand, similar accuracies and similar debris-covered ice outlines were obtained by the GB and

SVM_rbf classifiers (Fig. 11 and 13). In contrast, SVM_linear, DT, KNN, and MLP classifiers achieved lower accuracies. The lowest accuracy in our study was derived from the SVM_linear classifier, and it was mainly due to the nonlinear separability of the data. Another reason was the fact that these classifiers did not have a strong ability to work on the high dimensionality of data (Pal and Mather, 2003; Verleysen, 2003; Wang, 2011). Importantly, the results of this study further confirm that RF, GB, and SVM_rbf classifiers can successfully handle high data dimensionality (Pal, 2005; Lusa, 2015; Belgiu and Drăguţ, 2016). GB is learning from the many weak learning base classifiers (residual error) to create a strong predictive model to increase classification accuracy. RF decorrelates the trees with the introduction of splitting on a random subset of features, using a random subset of training samples, to improve classification accuracy. SVM is efficient for a two-class classification problem and it refers to the iterative process of finding a classifier with the maximum class boundary to separate the training patterns and perform the same configuration in high-dimensional space (Mountrakis et al., 2011). The above-mentioned properties may explain why RF, GB, and SVM_rbf have produced a significantly better classification accuracy. Areal comparisons of debris-covered ice outlines derived from MLCs and reference datasets (Fig. 7c1-c4 and Fig. 8c1-c3) indicated that various degrees of misclassification occurred in all MLCs classifiers in the glacier terminus region, where glacier ice is mostly covered by debris. These misclassifications likely occurred due to active stagnant ice that was exiting near the glacier tongue (Fig. 7b and 8b) or very thick debris cover on the glacier tongue with very low glacier motion.

Comparisons of area differences also revealed that the area difference between the RF, GB, SVM_rbf, and GE&Bhambri2017 maps was smaller compared to the RGI&GAMDAM (Fig. 12). The area difference between RF, GB, SVM_rbf, and RGI&GAMDAM are inappropriate to discuss here because RGI &GAMDAM outlines were generated by Landsat data around 1999/2000, therefore, it resulted in larger area differences (Fig. 12 and Table 2). This further illustrates that the automatic method is needed to regularly update the glacier inventory due to glaciers change, especially in response to the ongoing climate change or surge activity. The areal difference increased with a decrease in the debris-covered ice area.

Particularly, the larger area difference was observed (Glacier ID 6, 7, 9 Table 2) in smaller debris-covered ice areas (<1.0 km²). These indicated that the small debris-covered ice boundaries derived from this research had larger area differences compared to larger debris-covered ice (Fig. 12), indicating that 30 m resolution of the data was not good enough for the identification of smaller debris-covered ice areas with high accuracy. Minor misclassifications also occurred in glacier tongues, such as the river channel from glacier outlet, debris avalanche and debris-flow deposits (Fig. 12 c, e, and g) despite the fact that the automatic method took advantage of the coherence, thermal, terrain features from DEM, and spectral data. These errors can be ascribed to the effects of steep terrain on the SAR images, the lower resolution of the thermal band in comparison to the VNIR-SWIR bands, and thicker debris layer on the glacier terminated at the gentle slope.

6.3 Importance of hyper-parameters optimization

Hyper-parameters are important because they directly control the behavior of the MLCs, and can have a remarkable impact on classification accuracy. Therefore, the optimization of hyper-parameters was performed using cross-validation for MLCs. According to our hyper-parameters analysis optimization, RF classifiers showed a more robust parameter setting, faster and accurate for mapping debris-covered ice based on data used in this study (Belgiu and Drăguţ, 2016). GB classifier showed similar performance to RF despite its slightly lower accuracy. The SVM_rbf classifier had the third-highest classification accuracy, but was much slower in the tuning of hyper-parameters.

6.4 Comparisons with past studies

The past studies which focused on automated classification of debris-covered ice had some limitations that were addressed here. One limitation is that methodologies used in these studies were developed based on analysis of a single glacier or small study area, and therefore, applying these methods to other regions or larger glacierized areas are problematic (Brenning, 2009; Huang et al., 2014; Lippl et al., 2018). For example, accuracy was decreased (85% accuracy) (Robson et al., 2015) when a method developed for a smaller case study site was used to map debris-covered ice in a relatively larger area. Decreasing of accuracy occurred due to debris-covered ice classes was determined by a combination of results from SAR coherence, elevation, slope and spectral index which were derived by many thresholding values. Furthermore, MLCs classifiers such as SVM and RF were also used in past studies without hyper-parameter optimization. Hence, this study has several advantages compared to the previous studies: 1) It takes full advantage of coherence, thermal, topographic and, spectral futures to map debris-covered glaciers; 2) Our debris-coved ice map achieved 96% overall accuracy over a 2000 km² area using of freely available datasets like S1&S2, Landsat 8 and AW3D30 by an automatic process; 3) Seven MLCs were tested and examined to for debris-covered glacier classification; 4) Training data were obtained automatically based on existing glacier inventory data.

Multi-temporal (5 to 10 years) glacier inventories is still not available for many glacierized regions where changes are occurring rapidly (Paul et al., 2007). In the meantime, previous studies observed that debris cover on glacier surfaces has increased in recent decades (Bolch et al., 2012; Carturan et al., 2013; Tielidze et al., 2020). Importantly, the proposed MLC-based methods allow for mapping of the debris-covered ice areas accurately and (relatively) quickly, while having the advantage of transferability to other regions and other dates. Thus, the methods introduced in this study could help to fil the data gap in regions where few historical (and/or current) glacier inventory maps exist.

7. Conclusions

Regularly updated glacier inventories are essential for understanding glacier responses to climate change. However, debris layer on the glacier surface hampers the automatic, fast and accurate detection debris-covered ice. Therefore, this study introduced a new automatic classification scheme for hierarchical mapping of glacier areas based on the Machine learning classifiers, which takes advantage of optical, SAR, thermal and terrain features derived from freely available remote sensing datasets. The results derived from this study indicated that a combination of coherence, spectral, thermal and geomorphometric parameters allowed for the accurate detection of debris-covered glacier ice. For all classifiers tested, the misclassifications mainly occurred in the glacier terminus regions, which are typically fully covered by debris. The highest classification accuracy (97%) was achieved using the RF classifier. The RF classifier also was shown to be the most robust method to the parameter settings, enabling faster mapping of debris-covered ice. The GB classifier achieved the second-highest classification accuracy, but the difference in accuracy between RF and GB was quite small. SVM_rbf achieved the third-highest classification accuracy, but suffered from a much slower tuning of hyper-parameters.

Acknowledgment: This study was conducted in the Hirabayashi Lab, Shibaura Institute of technology. This paper was financially supported by MS&AD InterRisk Research & Consulting, Inc. and the Funding Program for the Global Environmental Research Fund (2-2005) by the Ministry of the Environment, Japan: The Integrated Research Program for Advancing Climate Models of the Ministry of Education, Culture, Sports, Science and Technology of Japan; and a grant-in-aid of scientific research (18H01540) from the Japan Society for the Promotion of Science. We are very grateful to the Japan Space Systems Earth Remote Sensing Division, the JAXA Earth Observation Research Center, NASA/USGS, and METI of Japan/NASA for providing the AW3D30, Landsat data and SRTM. We especially thank the ESA providing Sentinel-1 and Sentinel-2 data. Landsat series images and SRTM data were downloaded from the USGS Earth Explorer (EE) (USGS EE; http://earthexplorer.usgs.gov/). AW3D30 was obtained from the JAXA Earth Observation Research Center (EORC) (http://www.eorc.jaxa.jp/ALOS/en/aw3d30/data/index.htm). Sentinel-1/2 data were downloaded from Sentinels Scientific Data Hub (https://scihub.copernicus.eu/). Also, we thank Bhambri R. for sharing the glacier inventory data. We would like to thank the anonymous reviewers and the editor for their very constructive and helpful comments.

References

Alifu, H., Hirabayashi, Y., Johnson, B., Vuillaume, J.-F., Kondoh, A., Urai, M., 2018. Inventory of glaciers in the Shaksgam valley of the Chinese Karakoram mountains, 1970–2014. Remote Sens., 10(8), 1166.

Alifu, H., Tateishi, R., Johnson, B., 2015. A new band ratio technique for mapping debris-covered glaciers using Landsat imagery and a digital elevation model. Int J Remote Sens., 36(8), 2063-2075.

Altena, B., Scambos, T., Fahnestock, M., Kääb, A., 2019. Extracting recent short-term glacier velocity evolution over southern Alaska and the Yukon from a large collection of Landsat data. Cryosphere, 13(3), 795-814.

Altman, N.S., 1992. An introduction to kernel and nearest-neighbor nonparametric regression. Am. Stat., 46(3), 175-185.

Belgiu, M., Drăguţ, L., 2016. Random forest in remote sensing: A review of applications and future directions. ISPRS J. Photogramm., 114, 24-31.

Benn, D.I., Bolch, T., Hands, K.A., Gulley, J.D., Luckman, A., Nicholson, L.I., Quincey, D.J., Thompson, S., Toumi, R., Wiseman, S., 2012. Response of debris-covered glaciers in the Mount Everest region to recent warming, and implications for outburst flood hazards. Earth-Sci. Rev., 114(1-2), 156-174.

Bhambri, R., Bolch, T., Chaujar, R., 2011. Mapping of debris-covered glaciers in the Garhwal Himalayas using ASTER DEMs and thermal data. Int J Remote Sens., 32(23), 8095-8119.

Bhambri, R., Hewitt, K., Kawishwar, P., Pratap, B., 2017. Surge-type and surge-modified glaciers in the Karakoram. Sci. Rep., 7(1), 1-14.

Bishop, M.P., Bonk, R., Kamp Jr, U., Shroder Jr, J.F., 2001. Terrain analysis and data modeling for alpine glacier mapping. Polar Geogr., 25(3), 182-201.

Bolch, T., Buchroithner, M.F., Kunert, A., Kamp, U., 2007. Automated delineation of debris-covered glaciers based on ASTER data, Geoinformation in Europe. proceedings of the 27th EARSeL Symposium, pp. 4-6.

Bolch, T., Kamp, U., 2005. Glacier mapping in high mountains using DEMs, Landsat and ASTER data.

Bolch, T., Kulkarni, A., Kääb, A., Huggel, C., Paul, F., Cogley, J., Frey, H., Kargel, J.S., Fujita, K., Scheel, M., 2012. The state and fate of Himalayan glaciers. Science, 336(6079), 310-314.

Breiman, L., 2001. Random forests. Machine learning, 45(1), 5-32.

Brenning, A., 2009. Benchmarking classifiers to optimally integrate terrain analysis and multispectral remote sensing in automatic rock glacier detection. Remote Sens. Environ., 113(1), 239-247.

Brun, F., Berthier, E., Wagnon, P., Kääb, A., Treichler, D., 2017. A spatially resolved estimate of High Mountain Asia glacier mass balances from 2000 to 2016. Nat. Geosci., 10(9), 668-673.

Carturan, L., Baldassi, G.A., Bondesan, A., Calligaro, S., Carton, A., Cazorzi, F., Dalla Fontana, G., Francese, R., Guarnieri, A., Milan, N., 2013. Current behaviour and dynamics of the lowermost Italian glacier (Montasio Occidentale, Julian Alps). Geogr. Ann. A, Physical Geography, 95(1), 79-96.

Copland, L., Sylvestre, T., Bishop, M.P., Shroder, J.F., Seong, Y.B., Owen, L.A., Bush, A., Kamp, U., 2011. Expanded and Recently Increased Glacier Surging in the Karakoram. Arct. Antarct. Alp. Res., 43(4), 503-516.

Elith, J., Leathwick, J.R., Hastie, T., 2008. A working guide to boosted regression trees. J. Anim. Ecol., 77(4), 802-813.

Foody, G., 2004. Supervised image classification by MLP and RBF neural networks with and without an exhaustively defined set of classes. Int J Remote Sens., 25(15), 3091-3104.

Friedl, M.A., Brodley, C.E., 1997. Decision tree classification of land cover from remotely sensed data. Remote Sens. Environ., 61(3), 399-409.

Gardner, J.S., Hewitt, K., 1990. A surge of Bualtar Glacier, Karakoram Range, Pakistan: a possible landslide trigger. J. Glaciol., 36(123), 159-162.

Haapanen, R., Ek, A.R., Bauer, M.E., Finley, A.O., 2004. Delineation of forest/nonforest land use classes using nearest neighbor methods. Remote Sens. Environ., 89(3), 265-271.

Haeberli, W., Hoelzle, M., Paul, F., Zemp, M., 2007. Integrated monitoring of mountain glaciers as key indicators of global climate change: the European Alps. Ann. Glaciol., Vol 46, 2007, 46, 150-160.

Hsu, C.-W., Chang, C.-C., Lin, C.-J., 2003. A practical guide to support vector classification.
Huang, L., Li, Z., Tian, B.-s., Zhou, J.-m., Chen, Q., 2014. Recognition of supraglacial debris in the Tianshan Mountains on polarimetric SAR images. Remote Sens. Environ., 145, 47-54.
Johnson, B., Xie, Z., 2013. Classifying a high resolution image of an urban area using super-object information. ISPRS J. Photogramm., 83, 40-49.
Kavzoglu, T., Mather, P., 2003. The use of backpropagating artificial neural networks in land cover classification. Int J Remote Sens., 24(23), 4907-4938.
Kirkbride, M.P., 2011. Debris-covered glaciers, Encyclopedia of snow, ice and glaciers. Springer, pp. 190-192.
Lawrence, R., Bunn, A., Powell, S., Zambon, M., 2004. Classification of remotely sensed imagery using stochastic gradient boosting as a refinement of classification tree analysis. Remote Sens. Environ., 90(3), 331-336.
Le Bris, R., Paul, F., Frey, H., Bolch, T., 2011. A new satellite-derived glacier inventory for western Alaska. Ann. Glaciol., 52(59), 135-143.
Li, C., Wang, J., Wang, L., Hu, L., Gong, P., 2014a. Comparison of classification algorithms and training sample sizes in urban land classification with Landsat thematic mapper imagery. Remote Sens., 6(2), 964-983.
Li, M., Zang, S.Y., Zhang, B., Li, S.S., Wu, C.S., 2014b. A Review of Remote Sensing Image Classification Techniques: the Role of Spatio-contextual Information. Eur J Remote Sens., 47, 389-411.
Lippl, S., Vijay, S., Braun, M., 2018. Automatic delineation of debris-covered glaciers using InSAR coherence derived from X-, C-and L-band radar data: a case study of Yazgyl Glacier. J. Glaciol., 64(247), 811-821.
Liu, K., Song, C., Ke, L., Jiang, L., Pan, Y., Ma, R., 2019. Global open-access DEM performances in Earth's most rugged region High Mountain Asia: A multi-level assessment. Geomorphology, 338, 16-26.
Lusa, L., 2015. Boosting for high-dimensional two-class prediction. BMC bioinformatics, 16(1), 300.
Marzeion, B., Leclercq, P.W., Cogley, J.G., Jarosch, A.H., 2015. Brief Communication: Global reconstructions of glacier mass change during the 20th century are consistent. Cryosphere, 9(6), 2399-2404.
Maselli, F., Chirici, G., Bottai, L., Corona, P., Marchetti, M., 2005. Estimation of Mediterranean forest attributes by the application of k-NN procedures to multitemporal Landsat ETM+ images. Int J Remote Sens., 26(17), 3781-3796.
Mather, P., Tso, B., 2016. Classification methods for remotely sensed data. CRC press.
Maxwell, A.E., Warner, T.A., Fang, F., 2018. Implementation of machine-learning classification in remote sensing: an applied review. Int J Remote Sens., 39(9), 2784-2817.
Mölg, N., Bolch, T., Rastner, P., Strozzi, T., Paul, F., 2018. A consistent glacier inventory for the Karakoram and Pamir derived from Landsat data: distribution of debris cover and mapping challenges. Earth Syst. Sci. Data, 10, 1807-1827.
Mountrakis, G., Im, J., Ogole, C., 2011. Support vector machines in remote sensing: A review. ISPRS J. Photogramm., 66(3), 247-259.
Nakawo, M., Young, G.J., 1982. Estimate of glacier ablation under a debris layer from surface temperature and meteorological variables. J. Glaciol., 28(98), 29-34.
Nicholson, L., Benn, D.I., 2006. Calculating ice melt beneath a debris layer using meteorological data. J. Glaciol., 52(178), 463-470.
Nielsen, M.A., 2015. Neural networks and deep learning, 25. Determination press San Francisco, CA, USA:.
Opitz, D., Maclin, R., 1999. Popular ensemble methods: An empirical study. J. Artif. Intell. Res., 11, 169-198.
Östrem, G., 1959. Ice melting under a thin layer of moraine, and the existence of ice cores in moraine ridges. Geogr. Ann. A, 41(4), 228-230.

Pal, M., 2002. Factors influencing the accuracy of remote sensing classifications: a comparative study. PhD thesis, University of Nottingham.

Pal, M., 2005. Random forest classifier for remote sensing classification. Int J Remote Sens., 26(1), 217-222.

Pal, M., 2008. Ensemble of support vector machines for land cover classification. Int J Remote Sens., 29(10), 3043-3049.

Pal, M., Mather, P.M., 2003. An assessment of the effectiveness of decision tree methods for land cover classification. Remote Sens. Environ., 86(4), 554-565.

Paul, F., Barrand, N.E., Baumann, S., Berthier, E., Bolch, T., Casey, K., Frey, H., Joshi, S., Konovalov, V., Le Bris, R., and Mölg, N., 2013. On the accuracy of glacier outlines derived from remote-sensing data. Ann. Glaciol., 54(63), 171-182.

Paul, F., Huggel, C., Kääb, A., 2004. Combining satellite multispectral image data and a digital elevation model for mapping debris-covered glaciers. Remote Sens. Environ., 89(4), 510-518.

Paul, F., Kääb, A., Haeberli, W., 2007. Recent glacier changes in the Alps observed by satellite: Consequences for future monitoring strategies. Global Planet. Change, 56(1-2), 111-122.

Paul, F., Winsvold, S., Kääb, A., Nagler, T., Schwaizer, G., 2016. Glacier remote sensing using Sentinel-2. Part II: Mapping glacier extents and surface facies, and comparison to Landsat 8. Remote Sens., 8(7), 575.

Pedregosa, F., Varoquaux, G., Gramfort, A., Michel, V., Thirion, B., Grisel, O., Blondel, M., Prettenhofer, P., Weiss, R., Dubourg, V., 2011. Scikit-learn: Machine learning in Python. J. Mach. Learn. Res., 12(Oct), 2825-2830.

Pfeffer, W.T., Arendt, A.A., Bliss, A., Bolch, T., Cogley, J.G., Gardner, A.S., Hagen, J.O., Hock, R., Kaser, G., Kienholz, C., Miles, E.S., Moholdt, G., Molg, N., Paul, F., Radic, V., Rastner, P., Raup, B.H., Rich, J., Sharp, M.J., Andeassen, L.M., Bajracharya, S., Barrand, N.E., Beedle, M.J., Berthier, E., Bhambri, R., Brown, I., Burgess, D.O., Burgess, E.W., Cawkwell, F., Chinn, T., Copland, L., Cullen, N.J., Davies, B., De Angelis, H., Fountain, A.G., Frey, H., Giffen, B.A., Glasser, N.F., Gurney, S.D., Hagg, W., Hall, D.K., Haritashya, U.K., Hartmann, G., Herreid, S., Howat, I., Jiskoot, H., Khromova, T.E., Klein, A., Kohler, J., Konig, M., Kriegel, D., Kutuzov, S., Lavrentiev, I., Le Bris, R., Li, X., Manley, W.F., Mayer, C., Menounos, B., Mercer, A., Mool, P., Negrete, A., Nosenko, G., Nuth, C., Osmonov, A., Pettersson, R., Racoviteanu, A., Ranzi, R., Sarikaya, M.A., Schneider, C., Sigurdsson, O., Sirguey, P., Stokes, C.R., Wheate, R., Wolken, G.J., Wu, L.Z., Wyatt, F.R., Randolph, C., 2014. The Randolph Glacier Inventory: a globally complete inventory of glaciers. J. Glaciol., 60(221), 537-552.

Pham, T.D., Yoshino, K., Bui, D.T., 2017. Biomass estimation of Sonneratia caseolaris (l.) Engler at a coastal area of Hai Phong city (Vietnam) using ALOS-2 PALSAR imagery and GIS-based multi-layer perceptron neural networks. GISci. Remote Sens., 54(3), 329-353.

Pritchard, H.D., 2019. Asia’s shrinking glaciers protect large populations from drought stress. Nature, 569(7758), 649-654.

Qian, Y., Zhou, W., Yan, J., Li, W., Han, L., 2015. Comparing machine learning classifiers for object-based land cover classification using very high resolution imagery. Remote Sens., 7(1), 153-168.

Racoviteanu, A., Williams, M.W., 2012. Decision tree and texture analysis for mapping debris-covered glaciers in the Kangchenjunga area, Eastern Himalaya. Remote Sens., 4(10), 3078-3109.

Racoviteanu, A.E., Arnaud, Y., Williams, M.W., Ordonez, J., 2008. Decadal changes in glacier parameters in the Cordillera Blanca, Peru, derived from remote sensing. J. Glaciol., 54(186), 499-510.

Racoviteanu, A.E., Paul, F., Raup, B., Khalsa, S.J.S., Armstrong, R., 2009. Challenges and recommendations in mapping of glacier parameters from space: results of the 2008 Global Land Ice Measurements from Space (GLIMS) workshop, Boulder, Colorado, USA. Ann. Glaciol., 50(53), 53-69.

Rankl, M., Kienholz, C., Braun, M., 2014. Glacier changes in the Karakoram region mapped by multimission satellite imagery. Cryosphere, 8(3), 977-989.

Ranzi, R., Grossi, G., Iacovelli, L., Taschner, S., 2004. Use of multispectral ASTER images for mapping debris-covered glaciers within the GLIMS project, IGARSS 2004. 2004 IEEE International Geoscience and Remote Sensing Symposium. IEEE, pp. 1144-1147.

Rashid, I., Majeed, U., Jan, A., Glasser, N.F., 2020. The January 2018 to September 2019 surge of Shisper Glacier, Pakistan, detected from remote sensing observations. Geomorphology, 351, 106957.

Rastner, P., Bolch, T., Notarnicola, C., Paul, F., 2013. A comparison of pixel-and object-based glacier classification with optical satellite images. IEEE J. Sel. Top Appl. Earth Obs. Remote Sens., 7(3), 853-862.

RGI Consortium, 2017. Randolph Glacier Inventory – A Dataset of Global Glacier Outlines: Version 6.0: Technical Report, Colorado,USA. Digital Media.

Robson, B.A., Nuth, C., Dahl, S.O., Hölbling, D., Strozzi, T., Nielsen, P.R., 2015. Automated classification of debris-covered glaciers combining optical, SAR and topographic data in an object-based environment. Remote Sens. Environ., 170, 372-387.

Röhl, K., 2008. Characteristics and evolution of supraglacial ponds on debris-covered Tasman Glacier, New Zealand. J. Glaciol., 54(188), 867-880.

Rumelhart, D.E., Hinton, G.E., Williams, R.J., 1985. Learning internal representations by error propagation, California Univ San Diego La Jolla Inst for Cognitive Science.

Safavian, S.R., Landgrebe, D., 1991. A survey of decision tree classifier methodology. IEEE T. SYST. MAN CY., 21(3), 660-674.

Sakai, A., 2019. Brief communication: Updated GAMDAM glacier inventory over high-mountain Asia. Cryosphere, 13(7), 2043-2049.

Sarle, W., 2002. Neural Network FAQ, Part 2: "subject: should I normalize/standardize/rescale the data?". ftp://ftp.sas.com/pub/neural/FAQ2.html#A_std. Accessed 5 2019.

Schauwecker, S., Rohrer, M., Huggel, C., Kulkarni, A., Ramanathan, A., Salzmann, N., Stoffel, M., Brock, B., 2015. Remotely sensed debris thickness mapping of Bara Shigri glacier, Indian Himalaya. J. Glaciol., 61(228), 675-688.

Senese, A., Maragno, D., Fugazza, D., Soncini, A., D'Agata, C., Azzoni, R.S., Minora, U., Ul-Hassan, R., Vuillermoz, E., Asif Khan, M., 2018. Inventory of glaciers and glacial lakes of the Central Karakoram National Park (CKNP–Pakistan). J. MAPS, 14(2), 189-198.

Shi, Y., Liu, S., Ye, B., Liu, C., Wang, Z., 2008. Concise glacier inventory of China. Shanghai Popular Science Press, Shanghai, China.

Shukla, A., Arora, M., Gupta, R., 2010a. Synergistic approach for mapping debris-covered glaciers using optical–thermal remote sensing data with inputs from geomorphometric parameters. Remote Sens. Environ., 114(7), 1378-1387.

Shukla, A., Gupta, R., Arora, M., 2010b. Delineation of debris-covered glacier boundaries using optical and thermal remote sensing data. Remote Sens. Lett., 1(1), 11-17.

Steiner, J.F., Kraaijenbrink, P.D., Jiduc, S.G., Immerzeel, W.W., 2018. Brief communication: the Khurdopin glacier surge revisited–extreme flow velocities and formation of a dammed lake in 2017. Cryosphere, 12(1), 95-101.

Takaku, J., Tadono, T., Tsutsui, K., 2014. GENERATION OF HIGH RESOLUTION GLOBAL DSM FROM ALOS PRISM. ISPRS Annals of Photogrammetry, Remote Sensing & Spatial Information Sciences, 2(4).

Thanh Noi, P., Kappas, M., 2018. Comparison of random forest, k-nearest neighbor, and support vector machine classifiers for land cover classification using Sentinel-2 imagery. Sensors, 18(1), 18.

Tielidze, L.G., Bolch, T., Wheate, R.D., Kutuzov, S.S., Lavrentiev, I.I., Zemp, M., 2020. Supra-glacial debris cover changes in the Greater Caucasus from 1986 to 2014. Cryosphere.

Veci, L., Lu, J., Prats-Iraola, P., Scheiber, R., Collard, F., Fomferra, N., Engdahl, M., 2014. The Sentinel-1 Toolbox, Proceedings of the IEEE International Geoscience and Remote Sensing Symposium (IGARSS), pp. 1-3.

Verleysen, M., 2003. Learning high-dimensional data. Nato Science Series Sub Series III Computer And Systems Sciences, 186, 141-162.

Wang, X., 2011. A fast exact k-nearest neighbors algorithm for high dimensional search using k-means clustering and triangle inequality, The 2011 International Joint Conference on Neural Networks. IEEE, pp. 1293-1299.

Watanachaturaporn, P., Arora, M.K., Varshney, P.K., 2008. Multisource Classification Using Support Vector Machines. Photogramm Eng. Rem. S., 74(2), 239-246.

Yang, L., Mansaray, L.R., Huang, J., Wang, L., 2019. Optimal Segmentation Scale Parameter, Feature Subset and Classification Algorithm for Geographic Object-Based Crop Recognition Using Multisource Satellite Imagery. Remote Sens., 11(5), 514.

Yuan, H., Van Der Wiele, C., Khorram, S., 2009. An automated artificial neural network system for land use/land cover classification from Landsat TM imagery. Remote Sens., 1(3), 243-265.

Zhang, F., Du, B., Zhang, L., 2015. Scene classification via a gradient boosting random convolutional network framework. IEEE Trans. Geosci. Remote Sens., 54(3), 1793-1802.

Zhang, J., Jia, L., Menenti, M., Hu, G., 2019. Glacier Facies Mapping Using a Machine-Learning Algorithm: The Parlung Zangbo Basin Case Study. Remote Sens., 11(4), 452.

Declaration of competing interests

☒ The authors declare that they have no known competing financial interests or personal relationships that could have appeared to influence the work reported in this paper.

☐The authors declare the following financial interests/personal relationships which may be considered as potential competing interests:

Highlights

- Sentinel-1&2, Landsat 8 and AW3D30 data used to map debris-covered ice
- The highest accuracy achieved using the RF classifier
- GB classifier showed slightly lower accuracy compared to RF classifier
- SVM_rbf classifier had third-best accuracy despite low computation speed